Journal of Engineering Mathematics **38:** 323–354, 2000.

Wavelet methods for the solution of wave-body problems

JENS OLAV NYGAARD[1] and JOHN GRUE
Mechanics Division, Department of Mathematics, University of Oslo, Norway
e-mail: jnygaard@math.sintef.no; johng@math.uio.no

Received 22 December 1998; accepted in revised form 21 January 2000

Abstract. Fredholm integral equations of the second kind that arise in wave analysis of floating bodies are solved using a wavelet method. The two-dimensional linear wave-body problem for arrays of rectangular cylinders floating in the free surface of an otherwise unbounded fluid is considered. Both spline wavelets and the Daubechies wavelets with adaption to an interval are used as basis functions. An *a priori* compression strategy taking into account the singularities of the kernel of the integral equation, which arise at the corners of the geometry, is developed. The algorithm is $\mathcal{O}(n)$, where n is the number of unknowns. Computations of the hydrodynamic properties of the cylinders using the compression strategy are performed. The strategy is found to work well. A very high compression rate is obtained, still keeping a high accuracy of the computations. The accuracy of the potential close to the corners (singular points) is examined in a special case where an analytical solution is available.

Key words: integral equations, wavelets, high-order methods, compression, marine hydrodynamics

1. Introduction

Integral-equation methods represent powerful alternatives in computations of potential flow around geometries, where an important example is interaction between water waves and floating bodies. Numerical implementation of the integral equations has often been based on low-order methods, where the boundary of the geometry is subdivided into piecewise straight lines in two dimensions, or quadrilaterals in three dimensions. The unknown potential or source-strength is assumed to be constant over each subdivision of the boundary. For complex geometries like *e.g.*, the wetted part of an oil platform, this method leads to a large number of unknowns, if a reasonable accuracy of the potential and the flow shall be obtained, see, *e.g.*, [1–3].

The many applications of the low-order method illustrate its power. It is, however, desirable to investigate higher-order panel methods which have features not included in a low-order method. Desired features may be the possibility of finding derivatives of the potential, reduction of the number of unknowns and thereby the size of the matrices, fast convergence of the method, and adaptivity. Another aspect relates to geometrical design. Most practical geometries today are designed by advanced mathematical procedures, *e.g.*, the use of splines. It is therefore desirable to make available wave-analysis tools which are based on the same mathematical procedures as in the modelling of the geometry. The purpose is to integrate efficient and accurate computations of the flow and forces in the design process of, *e.g.*, marine structures.

[1]Present address: SINTEF Applied Mathematics, PB 124 Blindern, N-0314 Oslo, Norway.

Higher-order panel methods for analysis of wave-body interactions are presently under rapid development. Particularly we mention the application of spline and spline-Galerkin methods described in, *e.g.*, [4–5].

Here we shall investigate a different path, namely the application of wavelets in the form of a multiresolution analysis, to solve Fredholm integral equations of the second kind that arise in wave analysis of floating bodies. For simplicity we consider the linear two-dimensional problem. The geometries under consideration are arrays of rectangular cylinders floating in the free surface. In the multiresolution analysis we use biorthogonal cubic and linear spline wavelets developed by Mørken and Nygaard [6], see Section 3. The spline wavelets combine the properties of wavelets and splines. They are biorthogonal and have vanishing moments in addition to sharing the usual properties of ordinary splines. Application of the biorthogonal spline wavelets also involves a dual multiresolution analysis, where the wavelets of the latter are non-smooth, however. For comparison we also investigate the performance of the orthogonal Daubechies wavelets.

The property of vanishing moments of the wavelets makes possible a compression of the kernel of the integral equation ([7]), and we shall here investigate a certain *a priori compression strategy*. We proceed as follows: Typical for linear analysis of wave-body interactions is that a solution is required for several wavenumbers. The kernel of the integral equations under consideration is composed by a nonsingular wave part and a part which is independent of the wavenumber. The latter part is regular for smooth geometries but becomes singular if the geometry has one or more corners, and this is the case in our applications.

A compression, or 'sparsifying', strategy for a set of problems with different wavenumbers is then first to compute the entire (truncated) kernel for one of the wavenumbers in the range. For this wavenumber, we discard the smallest elements of the kernel and define from that a compression mask. For the remaining wavenumbers, where the kernel has no new singular properties, we compress the kernel *a priori* using the defined compression mask. The computational cost of solving the optimally compressed system is $\mathcal{O}(n)$, where n is the number of unknowns.

Computations of wave properties and hydrodynamic forces on arrays of rectangular cylinders are performed by means of the compression strategy. We always obtain a very high compression rate, still keeping a high accuracy of the computations. The accuracy of the potential close to the corners (singular points) is closely examined in a special case where an analytical solution is available. The cubic spline wavelets are found to have better properties than the linear spline wavelets. The application of the Daubechies wavelets is found to be not so efficient from a computational point of view.

The paper is organized as follows: In Section 2 the boundary-value problems are formulated. In Section 3 we discuss the multiresolution analysis and the wavelet bases. The solution of the integral equation is given in Section 4. The *a priori* compression strategy is described in Section 5. We illustrated the method in Section 6 by evaluating some hydrodynamic properties of arrays of rectangular cylinders, and Section 7 is a conclusion. We have added three appendices: Appendix A, describing the construction of a (biorthogonal) multiresolution analysis; B, the practical approximation in wavelet spaces; and C, the Schwarz–Christoffel mapping for the flow around a square cylinder.

2. The boundary-value problems

For simplicity we assume two-dimensional motion and consider half-immersed bodies in a free surface, either exposed to incoming waves or oscillating in otherwise calm water. We assume the fluid to be inviscid, incompressible and homogeneous, the motion irrotational, and the depth to be infinite. Coordinates (x, y) are introduced, with x being horizontal in the mean free surface and y vertical. If time harmonic motion with frequency ω is assumed, the potential is of the form

$$\Phi = \mathfrak{Re}(\hat{\chi} e^{i\omega t}), \tag{1}$$

where $\hat{\chi}$, according to the assumptions, satisfies the Laplace equation

$$\nabla^2 \hat{\chi} = 0 \tag{2}$$

in the fluid domain, for $y < 0$, $-\infty < x < \infty$. The free surface boundary condition is

$$\partial \hat{\chi} / \partial y = \nu \hat{\chi} \tag{3}$$

at $y = 0$, where $\nu = \omega^2/g$ denotes the wavenumber. Radiation conditions in the far field gives that the radiation and scattering potentials satisfy

$$\text{potential} \sim e^{\nu y \mp i\nu x} \quad \text{for} \quad x \to \pm\infty. \tag{4}$$

At the contour S_B of the body (bodies), we have for the radiation problem

$$\partial \hat{\chi} / \partial n = n_j, \tag{5}$$

where $n_1 = \boldsymbol{i} \cdot \boldsymbol{n}$ for the sway problem and $n_2 = \boldsymbol{j} \cdot \boldsymbol{n}$ for the heave problem. (For roll, $n_6 = x n_2 - y n_1$.) Here, $\boldsymbol{n} \equiv (n_1, n_2)$ is the unit normal vector pointing out of the fluid, and $\partial/\partial n$ denotes the directional derivative $\boldsymbol{n} \cdot \nabla(\cdot)$. For the diffraction problem, the boundary condition on S_B reads

$$\partial \hat{\chi} / \partial n = 0, \tag{6}$$

and we write

$$\hat{\chi} \equiv \hat{\chi}_D \frac{Aig}{\omega} = (\hat{\chi}_0 + \hat{\chi}_7) \frac{Aig}{\omega}, \tag{7}$$

where A denotes the amplitude of the incoming waves,

$$\hat{\chi}_0 = e^{\nu y - i\nu x} \tag{8}$$

denotes the (unit) incoming wave potential and $\hat{\chi}_7$ the scattering potential. By applying Green's theorem to $\hat{\chi}$ and the appropriate Green function, defined below in (14), we obtain the usual integral formulation for the radiation problem,

$$\int_{S_B} \left(\hat{\chi}(\boldsymbol{\xi}) \frac{\partial G(\boldsymbol{\xi}, \boldsymbol{x})}{\partial n_{\boldsymbol{\xi}}} - \frac{\partial \hat{\chi}(\boldsymbol{\xi})}{\partial n_{\boldsymbol{\xi}}} G(\boldsymbol{\xi}, \boldsymbol{x}) \right) \mathrm{d}S_{\boldsymbol{\xi}} = \begin{cases} -\pi \hat{\chi}(\boldsymbol{x}) & \text{on} \quad S_B \\ -2\pi \hat{\chi}(\boldsymbol{x}) & \text{in the fluid} \end{cases} \tag{9}$$

where $\boldsymbol{\xi} = (\xi, \eta)$, $\boldsymbol{x} = (x, y)$. The equations for the diffraction problem become

$$\int_{S_B} \hat{\chi}_D(\boldsymbol{\xi}) \frac{\partial G(\boldsymbol{\xi}, \boldsymbol{x})}{\partial n_{\boldsymbol{\xi}}} \, \mathrm{d}S_{\boldsymbol{\xi}} - 2\pi \hat{\chi}_0(\boldsymbol{x}) = \begin{cases} -\pi \hat{\chi}_D(\boldsymbol{x}) & \text{on } S_B \\ -2\pi \hat{\chi}_D(\boldsymbol{x}) & \text{in the fluid} \end{cases} . \tag{10}$$

We introduce a parametrisation

$$\boldsymbol{x} = (p_1(t), p_2(t)), \boldsymbol{\xi} = (p_1(u), p_2(u)), \tag{11}$$

and may then write (9) and (10) as

$$\chi(t) = \int_0^1 K(t,u)\chi(u) \, \mathrm{d}u + H(t), \tag{12}$$

$$\chi_D(t) = \int_0^1 K(t,u)\chi_D(u) \, \mathrm{d}u + H_D(t). \tag{13}$$

We solve independently (12) with χ as unknown for the radiation problem, and (13) with $\hat{\chi}_D$ as unknown for the diffraction problem.

The wave Green function satisfying Laplace's equation (2) and the boundary conditions (3) and (4), given in Wehausen and Laitone [8, Equations 13.22–13.28], reads

$$G(\boldsymbol{\xi}, \boldsymbol{x}) = \log r - \log r_1 + 2\mathfrak{Re}\left(\mathrm{e}^Z \int_\infty^Z \frac{\mathrm{e}^{-w}}{w} \, \mathrm{d}w \right) + 2\pi \mathrm{i} \mathrm{e}^Z, \tag{14}$$

where $r = [(x-\xi)^2+(y-\eta)^2]^{1/2}$, $r_1 = [(x-\xi)^2+(y+\eta)^2]^{1/2}$, and $Z = -\mathrm{i}\nu(\xi-x)+\nu(\eta+y)$, $-3\pi/2 < \arg(Z) < -\pi/2$. Then,

$$K(t,u) = \Bigg[\frac{(\xi-x)n_1 + (\eta-y)n_2}{r^2} - \frac{(\xi-x)n_1 + (\eta+y)n_2}{(r_1)^2}$$

$$+ 2\nu\mathfrak{Re}\left\{ \left(\mathrm{e}^Z \int_\infty^Z \frac{\mathrm{e}^{-w}}{w} \, \mathrm{d}w + \frac{1}{Z} \right) (-\mathrm{i}n_1 + n_2) \right\} \tag{15}$$

$$+ 2\nu\pi \mathrm{i} \mathrm{e}^Z (-\mathrm{i}n_1 + n_2) \Bigg] \sqrt{\xi'^2 + \eta'^2} \tag{16}$$

and

$$H(t) = \int_0^1 n_j \left[\log r - \log r_1 + 2\mathrm{e}^Z \mathfrak{Re}\left(\int_\infty^Z \frac{\mathrm{e}^w}{w} \, \mathrm{d}w \right) + 2\pi \mathrm{i} \mathrm{e}^Z \right] \sqrt{\xi'^2 + \eta'^2} \, \mathrm{d}u, \tag{17}$$

$$H_D(t) = 2\pi \mathrm{e}^{\nu y - \mathrm{i}\nu x}, \tag{18}$$

where $n_j = n_1$ for the sway problem and $n_j = n_2$ for the heave problem. All coordinate functions depend on the parameters t and u, and $\xi' = \mathrm{d}p_1(u)/\mathrm{d}u$ and $\eta' = \mathrm{d}p_2(u)/\mathrm{d}u$.

3. The wavelet method – multiresolution analysis

We shall solve the integral equations (12) and (13) making use of a *wavelet method*. This is done by expanding the unknown potential, the kernel, and the right-hand side of the integral equation in a *multiresolution analysis*, see, *e.g.*, [9, pp. 129–167] and [10]. We will use the terms *multiresolution analysis* and *wavelet basis* interchangeably. The wavelets we apply are spline wavelets [6] and the Daubechies wavelets [9, pp. 167–215]. Briefly, expanding a function f in a multiresolution analysis means that f is decomposed as

$$f = f_0 + g_0 + g_1 + \cdots = \sum_k c_k^0 \phi_k^0 + \sum_k d_k^0 \psi_k^0 + \sum_k d_k^1 \psi_k^1 + \cdots , \tag{19}$$

where the functions g_j are corrections to a remainder f_0, capturing different frequencies. In (19), we have introduced the *scaling functions* ϕ_k^j and the *wavelet functions* ψ_k^j. These functions are the translated and scaled versions of the so-called *mother scaling function* ϕ and the *mother wavelet* ψ, and they are given by

$$\phi_k^j(t) = 2^{j/2}\phi(2^j t - k), \tag{20}$$

$$\psi_k^j(t) = 2^{j/2}\psi(2^j t - k). \tag{21}$$

(We keep the superscript j for the purpose of making a smoother transition into the next section.) The functions ϕ_k^0 span a space V_0, and the multiresolution analysis consists of a sequence of nested spaces $\cdots \subset V_{-1} \subset V_0 \subset V_1 \subset \cdots$. Two properties of the multiresolution analysis are that $f \in V_j \Leftrightarrow f(2x) \in V_{j+1}$ (scaling) and $f(x) \in V_0 \Leftrightarrow f(x-k) \in V_0$ (translation). From this it follows that $\{\phi_k^j\}$ forms a basis of V_j for all j. Likewise, $\{\psi_k^j\}$ forms a basis for the *wavelet space* W_j defined as the complement of V_j in V_{j+1}, such that $V_j + W_j = V_{j+1}$. If the function f of (19) is in V_j, we now see that f is decomposed into an approximation f_0 with increasingly finer corrections $g_0, \ldots, g_{j-1}$.

The action of combining the functions $f_j \in V_j$ and $g_j \in W_j$ into $f_{j+1} \in V_{j+1}$ is called *reconstruction*, while the splitting of f_{j+1} into f_j and g_j is called *decomposition*. For wavelets with compact support, these are fast procedures (filter operations) of order $\mathcal{O}(m \cdot n)$ where n is the number of basis functions spanning the space, and m is the filter length (length of the support of the mother wavelet.)

The situation described corresponds to functions defined on all of $\mathbb{R}$, and $k \in \mathbb{Z}$. For functions on an interval, which we use, additional (and modified) scaling and wavelet functions near the ends of the interval, *end functions*, are required. For the Daubechies wavelets, we use the modification due to Cohen *et al.* [11], and for the biorthogonal spline wavelets, we use the construction of Mørken and Nygaard [6]. Further details are given in Appendix A.

We define the inner product $\langle f, g\rangle \equiv \int_0^1 f(t)g(t)\,\mathrm{d}t$ and assume the interval under consideration to be [0, 1]. The coefficients c_k^j and d_k^j in (19) are obtained by

$$c_k^j = \langle f, \tilde{\phi}_k^j\rangle, \quad d_k^j = \langle f, \tilde{\psi}_k^j\rangle,$$

where the multiresolution analysis given by ϕ and ψ, together with a *dual multiresolution analysis*, determined by the dual scaling function $\tilde{\phi}$ and the dual wavelet $\tilde{\psi}$, constitute a *biorthogonal multiresolution analysis*. (See also Appendix B for the computation of the c_k^j and d_k^j.) The scaling and wavelet functions of the dual multiresolution analysis span corresponding spaces $\tilde{V}_j$ and $\tilde{W}_j$, where

$$\tilde{V}_j \perp W_j, \quad V_j \perp \tilde{W}_j,$$

and

$$\langle \tilde{\phi}, \phi(\cdot - k)\rangle = \langle \tilde{\psi}, \psi(\cdot - k)\rangle = \begin{cases} 1, & k = 0 \\ 0, & k \neq 0 \end{cases}.$$

(When $\tilde{\phi} = \phi$ and $\tilde{\psi} = \psi$, we have an *orthogonal* multiresolution analysis, *e.g.*, the Daubechies multiresolution analysis.) We note that an orthogonal wavelet basis constitutes its own dual basis, and that the role of a basis and its dual may be interchanged if they span the same approximation spaces.

Finally, we note that a wavelet ψ is said to have N vanishing moments when

$$\langle \psi, x^m \rangle = 0, \quad m = 0, \ldots, N-1,$$

and $\langle \psi, x^N \rangle \neq 0$ are satisfied. This property we shall later make use of.

3.1. Biorthogonal spline wavelets

As mentioned, we will primarily use a particular set of *biorthogonal wavelets*, the biorthogonal spline wavelets developed in [6]. These wavelets are constructed within the framework of the lifting scheme, see [12] and [13].

This basis of spline wavelets has many advantages, not the least being the connection to splines, considering the extensive use of spline bases in other contexts, *e.g.*, for the modelling of geometries. The application of these wavelets can be regarded as an extension of the use of splines. We have nested approximation spaces spanned by splines, and the differences between these spaces are the wavelet spaces. For examples of the spline wavelet basis functions, see Figure 1. (In order to plot these basis functions, they are *lifted* from a coarse space to a finer, say V_J, and then the coefficients are plotted. Note that in the case of the dual functions (c) and (d) of Figure 1, this *cascade algorithm* does not converge in L^∞, although it does converge in L^2, see [9, pp. 202–213].)

By not restricting the dual functions to be splines, we can also make the support of the dual function compact (of finite length), making possible an efficient implementation. For spline wavelets of degree d with N vanishing moments, we have that the support of the scaling function has length $d + 1$ and the support of the wavelet has length $d + N$. The corresponding supports of the dual scaling function and the dual wavelet are $d + 2N - 1$ and $d + N$, respectively. (A support of length m means that m adjacent basis functions overlap each other, and that the decomposition and reconstruction from one level j to one below or above can be performed by a convolution with a filter of length m.)

From Figures 1 and 2 we see that the dual scaling functions and dual wavelets typically are less smooth than the scaling functions and wavelets. On the other hand, the smoothness increases with the number of vanishing moments. In practice, lack of smoothness in the dual bases is not a problem, because only the kernel of the integral equations will be expanded in the tensor product of the non-dual and the dual multiresolution analysis, while the unknown potential will be expanded in the smooth spline wavelets.

The spline wavelets have another nice property which the Daubechies bases do not have, namely that they are symmetric. Finally, the construction of the biorthogonal spline wavelets has made the construction of coarse wavelet spaces (with few basis functions) easier than in the case of the interval-adaption of the Daubechies bases. This is important for problems with complex geometries with moderate accuracy requirements of the solution.

3.2. The Daubechies basis

By using the somewhat stronger restriction of orthogonality, and also requiring that the wavelets have the shortest possible support, one obtains the *Daubechies wavelets*, see [9, pp. 167–215].

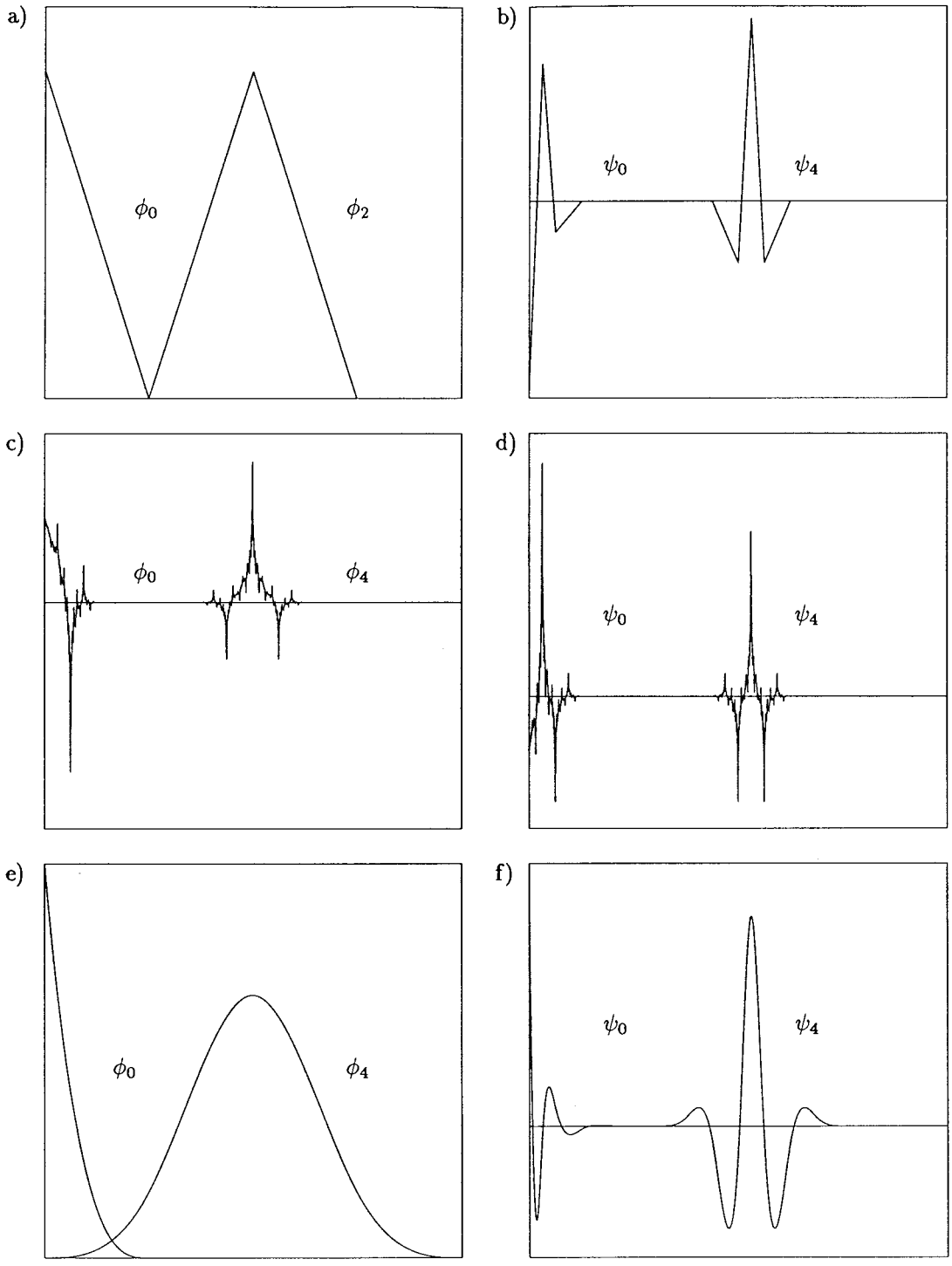

Figure 1. The leftmost and inner linear spline scaling functions ϕ_k (a), wavelets ψ_k with two vanishing moments (b), dual scaling functions $\tilde{\phi}_k$ with two vanishing moments (c), dual wavelets $\tilde{\psi}_k$ with two vanishing moments (d), cubic spline scaling functions ϕ_k (e), and corresponding wavelets with four vanishing moments (f).

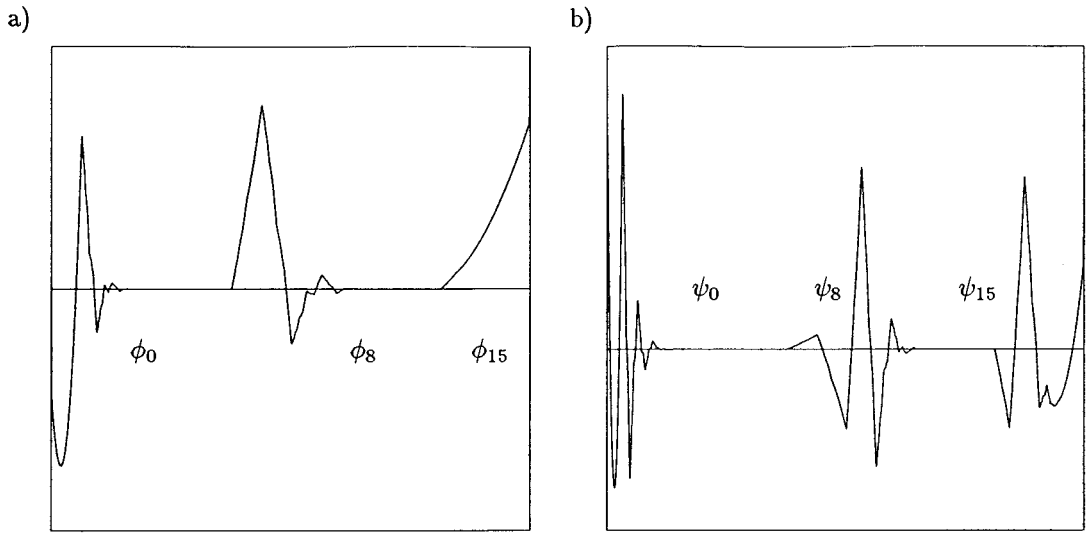

Figure 2. The leftmost, inner and the rightmost scaling functions ϕ_0, ϕ_8 and ϕ_{15} (a), and the leftmost, inner and rightmost wavelet functions ψ_0, ψ_8 and ψ_{15} (b), of the modified Daubechies basis for $N = 3$.

Even though orthogonality and short support are desirable features, two disadvantages of the Daubechies wavelets are that the scaling functions and wavelets are non-symmetric, and that they for small N are less smooth than *e.g.*, the spline wavelet basis. The scaling and wavelet functions of the basis with N vanishing moments have support with length $2N - 1$. However, their smoothness is asymptotically $C^{\mu N}$ ($N \to \infty$) where $\mu \approx 0 \cdot 2$, see [9, p. 242]. In order to get a basis for functions on an interval we have made use of the adaption to an interval described by Cohen *et al.* [11]. Some of the scaling and wavelet functions for this basis, for $N = 3$, are depicted in Figure 2. The inner functions are not very smooth, but since they have three vanishing moments the approximation spaces include polynomials up to quadratic degree. The end functions are in fact piecewise polynomial themselves on parts of their supports.

Being orthogonal, the application of the Daubechies wavelets to the integral equation will be slightly simplified. In computations we use the Daubechies basis with $N = 3$ vanishing moments, for which we have been able to obtain precomputed filter cofficients.

4. Solution of the integral equations

We now apply the method based on the multiresolution analysis to the integral equations (12) and (13). We truncate and expand the unknown potential χ and the function H in the basis of V_J, *i.e.*, the *finest level*, and get $\bar{\chi}$ and $\bar{H}$. We then expand $\bar{\chi}$ and $\bar{H}$ in the spaces $W_{J-1}, \ldots, W_0$ and V_0, and denote these expansions as the *(wavelet) decompositions* of $\bar{\chi}$ and $\bar{H}$. This gives

$$\bar{\chi} = \sum_k c^J_{\chi,k} \phi^J_k \tag{22}$$

$$= \sum_{j=0}^{J-1} \sum_k d^j_{\chi,k} \psi^j_k + \sum_k c^0_{\chi,k} \phi^0_k = \sum_{j=0}^{J-1} \boldsymbol{\psi}^{jT} \boldsymbol{d}^j_\chi + \boldsymbol{\phi}^{0T} \boldsymbol{c}^0_\chi,$$

$$\bar{H} = \sum_k c^J_{H,k}\phi^J_k \tag{23}$$

$$= \sum_{j=0}^{J-1}\sum_k d^j_{H,k}\psi^j_k + \sum_k c^0_{H,k}\phi^0_k = \sum_{j=0}^{J-1} \boldsymbol{\psi}^{j_T}\boldsymbol{d}^j_H + \boldsymbol{\phi}^{0_T}\boldsymbol{c}^0_H, \tag{24}$$

where

$$\boldsymbol{\psi}^j = (\psi^j_0, \psi^j_1, \ldots, \psi^j_{2^j-1})^T, \quad \boldsymbol{\phi}^j = (\phi^j_0, \phi^j_1, \ldots, \phi^j_{2^j-1})^T, \tag{25}$$

$$\boldsymbol{d}^j_\chi = (d^j_{\chi,0}, d^j_{\chi,1}, \ldots, d^j_{\chi,2^j-1})^T, \quad \boldsymbol{c}^j_\chi = (c^j_{\chi,0}, c^j_{\chi,1}, \ldots, c^j_{\chi,2^j-1})^T, \tag{26}$$

and $(\cdot)^T$ denotes transposition. We define $\boldsymbol{d}^j_H$ and $\boldsymbol{c}^j_H$ similarly to $\boldsymbol{d}^j_\chi$ and $\boldsymbol{c}^j_\chi$. (In (25) and (26), we have introduced $\boldsymbol{\phi}^j$ and $\boldsymbol{c}^j_\chi$, $j > 0$, for later use.)

We next expand the kernel in the two-dimensional tensor-product of the one-dimensional non-dual and dual multiresolution analysis, *i.e.*, we project the kernel $K(t,u)$ onto the space $V_J \times \tilde{V}_J$ and decompose into the different wavelet spaces. Generalisation of a one-dimensional multiresolution analysis to higher dimensions is treated in, *e.g.*, [10]. For the truncated kernel, we obtain

$$\bar{K}(t,u) = \sum_{k,l} c_{J,k,l}\phi^J_k(t)\tilde{\phi}^J_l(u) \tag{27}$$

$$= \sum_{j=1}^{J-1}\sum_{k,l}\left[d^h_{j,k,l}\psi^j_k(t)\tilde{\phi}^j_l(u) + d^v_{j,k,l}\phi^j_k(t)\tilde{\psi}^j_l(u) + d^d_{j,k,l}\psi^j_k(t)\tilde{\psi}^j_l(u)\right]$$

$$+ \sum_{k,l} c_{0,k,l}\phi^0_k(t)\tilde{\phi}^0_l(u) \tag{28}$$

$$= \sum_{j=1}^{J-1}\left[\boldsymbol{\psi}^j(t)^T D^h_j \tilde{\boldsymbol{\phi}}^j(u) + \boldsymbol{\phi}^j(t)^T D^v_j \tilde{\boldsymbol{\psi}}^j(u) + \boldsymbol{\psi}^j(t)^T D^d_j \tilde{\boldsymbol{\psi}}^j(u)\right]$$

$$+ \boldsymbol{\phi}^0(t)^T C_J \tilde{\boldsymbol{\phi}}^0(u), \tag{29}$$

where k and l are to be summed from 0 to $K_j - 1$, and we have introduced the matrices $D^h_j = (d^h_{j,k,l})_{k,l}$, $D^v_j = (d^v_{j,k,l})_{k,l}$, $D^d_j = (d^d_{j,k,l})_{k,l}$ and $C_j = (c_{j,k,l})_{k,l}$. Using the biorthogonality, (orthogonality in the Daubechies case), we get

$$c_{j,k,l} = \iint K(t,u)\tilde{\phi}^j_k(t)\phi^j_l(u)\,\mathrm{d}t\,\mathrm{d}u, \tag{30}$$

$$d^h_{j,k,l} = \iint K(t,u)\tilde{\psi}^j_k(t)\phi^j_l(u)\,\mathrm{d}t\,\mathrm{d}u, \tag{31}$$

$$d^v_{j,k,l} = \iint K(t,u)\tilde{\phi}^j_k(t)\psi^j_l(u)\,\mathrm{d}t\,\mathrm{d}u, \tag{32}$$

$$d^d_{j,k,l} = \iint K(t,u)\tilde{\psi}^j_k(t)\psi^j_l(u)\,\mathrm{d}t\,\mathrm{d}u, \tag{33}$$

where the integrals are to be taken over the support of the integrands.

Equivalent to this approximation of the kernel is the approach where one uses the same approximation (22) of the unknown and then seek the solution which makes the residuals zero when weighted by the duals as test functions.

In the computational procedure we first find the coefficients $c^J_{H,k}$ of the expansion (24) for $\bar{H}$, *i.e.*,

$$c^J_{H,k} = 2^{J/2}\int H(t)\tilde{\phi}(2^J t - k)\,\mathrm{d}t, \tag{34}$$

and the coefficients $c_{J,k,l}$ of the expansion (27) for $\bar{K}$, *i.e.*,

$$c_{J,k,l} = \iint K(t,u)\tilde{\phi}^J_k(t)\phi^J_l(u)\,\mathrm{d}t\,\mathrm{d}u, \tag{35}$$

see Appendix B. To find the coefficients $c^j_{H,k}$, $d^j_{H,k}$ of (23) and the coefficients $c_{j,k,l}$, $d^h_{j,k,l}$, $d^v_{j,k,l}$, $d^d_{j,k,l}$ of (28), for $j < J$, we successively apply the decomposition algorithm, which is given by the filter coefficients for the particular wavelet bases.

Introducing

$$\bar{\boldsymbol{\chi}} = (\boldsymbol{d}^{J-1T}_\chi, \boldsymbol{d}^{J-2T}_\chi, \cdots, \boldsymbol{d}^{0T}_\chi, \boldsymbol{c}^{0T}_\chi)^T \quad \text{and} \quad \bar{\boldsymbol{H}} = (\boldsymbol{d}^{J-1T}_H, \boldsymbol{d}^{J-1T}_H, \cdots, \boldsymbol{d}^{0T}_H, \boldsymbol{c}^{0T}_H)^T, \tag{36}$$

and, using (29), we may write the discretized version of the integral equation (12) as

$$\bar{\boldsymbol{\chi}} - \bar{T}\bar{\boldsymbol{\chi}} = \bar{\boldsymbol{H}}, \tag{37}$$

where $\bar{T}\bar{\boldsymbol{\chi}}$ is given by

$$\begin{aligned}(\bar{T}\bar{\chi})(t) &= \int \bar{K}(t,u)\bar{\chi}(u)\,\mathrm{d}u \\ &= \sum_{j=1}^{J-1}\left[\boldsymbol{\psi}^j(t)^T(D^h_j\boldsymbol{c}^j_\chi + D^d_j\boldsymbol{d}^j_\chi) + \boldsymbol{\phi}^j(t)^T D^v_j\boldsymbol{d}^j_\chi\right] + \boldsymbol{\phi}^0(t)^T C_0\boldsymbol{c}^j_\chi.\end{aligned} \tag{38}$$

By expanding $\bar{K}$ in the non-dual and the dual multiresolution analysis, we see that both orthogonal and biorthogonal bases fit into the scheme. We note that the right-hand side of (38) is not of the form of a function decomposed in the multiresolution analysis, like (23), due to the terms $\boldsymbol{\phi}^j(t)^T D^v_j\boldsymbol{d}^j_\chi$, for $j > 0$. In order to get the projection of $(\bar{T}\bar{\chi})$ in (38) onto $W_{J-1}\oplus\cdots\oplus W_0\oplus V_0$, we iteratively decompose $\boldsymbol{\phi}^j(t)^T D^v_j\boldsymbol{d}^j_\chi$ for all $j > 0$.

The operator $\bar{T}$ may then be written as $\bar{T} = L\bar{T}_{NS}L^T$, where L is the composition of the decompositions from V_J down to the coarsest space V_0. This is implemented as matrix multiplications where the sparsity of the matrices is accounted for. The matrix $\bar{T}_{NS}$ contains the successive two-dimensional wavelet decompositions of the truncated kernel $\bar{K}(t,u)$, and $\bar{T}_{NS}$ on *non-standard form* ([7], for a different kernel) is then given by

$$\bar{T}_{NS} = \begin{pmatrix} 0 & D^v_{J-1} & & & & & \\ D^h_{J-1} & D^d_{J-1} & & & & & \\ & & \ddots & & & & \\ & & & 0 & D^v_1 & & \\ & & & D^h_1 & D^d_1 & & \\ & & & & & C_0 & D^v_0 \\ & & & & & D^h_0 & D^d_0 \end{pmatrix}, \tag{39}$$

where the empty parts contain zeros. (At the coarsest level $j = 0$, C_0, D^v_0, D^h_0 and D^d_0 may be scalars for the unmodified Daubechies basis, suitable for periodic problems.)

Since the resulting system (37) of equations in general is non-symmetric, we have chosen to use the method of generalised conjugate residuals, without truncation or restart (GCR(∞)), as described in [14, Chapter 3]. Without any explicit preconditioning, the size of the residual evaluated in L^2-norm reaches a prescribed level of precision (10^{-10}) typically after about 20–30 iterations. The number of iterations is found to be independent of the number n of unknowns, for the present examples. (Results not shown.) In the next section we will see that the cost of each step in the iteration is proportional to n for an optimally compressed, or sparsified, system. Other iterative solvers based on the application of the discretized integral operator (38) could also be used, as it is this operator which is optimized by the compression of its elements.

5. Compression strategy

We now make use of the vanishing moments of the wavelets in computing the matrix elements of (39). Consider, for example, the matrix elements $d^h_{j,k,l}$. We note that the kernel (16) can be decomposed by $K = K_1 + K_2$ where

$$K_1 = \frac{(\xi - x)n_1 + (\eta - y)n_2}{r^2}\sqrt{\xi'^2 + \eta'^2} = -\frac{\cos(\boldsymbol{r}, \boldsymbol{n})}{r}\sqrt{\xi'^2 + \eta'^2}, \tag{40}$$

and $\boldsymbol{r} = \boldsymbol{x} - \boldsymbol{\xi}$, $K_2 = K - K_1$. For a smooth contour, $\cos(\boldsymbol{r}, \boldsymbol{n})/r$ is smooth for $r \to 0$;

$$\lim_{r\to 0} -\frac{\cos(\boldsymbol{r}, \boldsymbol{n})}{r}\sqrt{\xi'^2 + \eta'^2} = -\frac{1}{2}(p_1'' p_2' - p_2'' p_1')\sqrt{\xi'^2 + \eta'^2}, \tag{41}$$

where (p_1, p_2) is the parametrisation (11) of the contour. For a contour with a corner, however, K_1 behaves like $\mathcal{O}(1/r)$ when $r \to 0$, which means that K_1 in this case is singular.

The remainder of the kernel, K_2, is not singular (for points below the free surface). This suggests that we write

$$\begin{aligned} d^h_{j,k,l} &= \iint K(t,u)\tilde{\psi}^j_k(t)\phi^j_l(u)\,\mathrm{d}t\,\mathrm{d}u \\ &= \iint K_1(t,u)\tilde{\psi}^j_k(t)\phi^j_l(u)\,\mathrm{d}t\,\mathrm{d}u + \iint K_2(t,u)\tilde{\psi}^j_k(t)\phi^j_l(u)\,\mathrm{d}t\,\mathrm{d}u. \end{aligned}$$

Consider now a parameter domain, where $K_1(t,u)$ is smooth enough to be expanded in a Taylor series in t about $t_0 = 2^{-j}k$, keeping u fixed. This will be when the geometry has no corner for any t or u in the support of $\tilde{\psi}_k^j(t)$ or $\phi_l^j(u)$. We can then expand $K = K_1 + K_2$, and insert the expansion into (42), and (making use of the vanishing moments) it follows that

$$d_{j,k,l}^h = \frac{2^j}{N!} \iint \frac{\partial^N K}{\partial t^N}(\tau, u)(t - t_0)^N \tilde{\psi}(2^j t - k)\phi(2^j u - l)\, \mathrm{d}t\, \mathrm{d}u, \tag{43}$$

for some $\tau \in \mathrm{support}\tilde{\psi}_k^j$.

Introducing $I^{\tilde{\psi}} = \mathrm{support}(\tilde{\psi})$, $I_{j,k}^{\tilde{\psi}} = \mathrm{support}(\tilde{\psi}_k^j)$, $I^{\phi} = \mathrm{support}(\phi)$, and $I_{j,l}^{\phi} = \mathrm{support}(\phi_l^j)$, we find that

$$|d_{j,k,l}^h| \le \frac{2^j}{N!} \sup_{\tau \in I_{j,k}^{\tilde{\psi}}, u \in I_{j,l}^{\phi}} \left| \frac{\partial^N K}{\partial t^N}(\tau, u) \right| \sup|\tilde{\psi}| \sup|\phi| \iint (t - t_0)^N \, \mathrm{d}t \, \mathrm{d}u. \tag{44}$$

We have $\iint (t - t_0)^N \, \mathrm{d}t \, \mathrm{d}u = |I_{j,k}^{\tilde{\psi}}|^{N+2}/(N+1)$. Since $|I_{j,k}^{\tilde{\psi}}| = 2^{-j}|I^{\tilde{\psi}}|$, we obtain

$$|d_{j,k,l}^h| \le \varepsilon_{j,k,l} \tag{45}$$

where

$$\varepsilon_{j,k,l} \equiv \frac{2^{-j(N+1)}}{(N+1)!} |I^{\tilde{\psi}}|^{N+2} \sup_{\tau \in I_{j,k}^{\tilde{\psi}}, u \in I_{j,l}^{\phi}} \left| \frac{\partial^N K}{\partial t^N}(\tau, u) \right| \sup|\tilde{\psi}| \sup|\phi|.$$

A similar analysis for the other coefficients may be carried out. This illustrates that the coefficients corresponding to the parts of the parameter space where the kernel is smooth, will be small, and that the greater the number of vanishing moments, the smaller these elements will be.

When K has singularities in the support of $\tilde{\psi}_k^j(t)$ or $\phi_l^j(u)$, we cannot compress this matrix element. However, when we are sufficiently far away from any singularity (corner), it will be small enough to be discarded.

A typical feature of water wave problems, is the need for solving the problem for a range of frequencies. We have decomposed the kernel into a singular part K_1 and a regular part K_2, where K_1 does not depend on the wavenumber ν, only on the geometry. We have seen that the compression is done by discarding elements for which the basis functions do not have singularities in their supports. This leads to the following compression strategy for a set of problems with different wavenumbers:

1. Compute the entire matrix for one of the wavenumbers in the range. We will do this for the largest wavenumber in the range, because this has the largest contributing K_2.
2. Compress *a posteriori* by discarding the smallest elements. Store the compression mask thus obtained.
3. For the remaining wavenumbers, compress the matrices *a priori* by using the compression mask.

5.1. Numerical results for the compression strategy

In order to illustrate the *a priori* compression strategy we perform computations of the kernel $\bar{K}$ for two floating rectangular cylinders, namely geometry B, depicted in Figure 5 in Section 6. The results are shown in Figures 3 (cubic spline wavelets) and 4 (linear spline wavelets), where the matrix (39) is organised as follows;

$$\begin{pmatrix} C_0 & D_0^v & D_1^v & & \\ D_0^h & D_0^d & & D_2^v & D_3^v \\ & D_1^h & D_1^d & & \\ & & D_2^h & D_2^d & \\ & & & D_3^h & D_3^d \end{pmatrix}. \tag{46}$$

Each matrix element is given an intensity proportional to the logarithm of its size. The darkest pixels correspond to the largest matrix elements, which will be retained. The smallest elements (brightest pixels) are the ones which will be discarded by the compression. We see the large $d^v_{j,k,l}$, $d^h_{j,k,l}$ and $d^d_{j,k,l}$ values caused by the corners of the geometry. Besides the elements in C_0, those are exactly the elements retained when compression is applied. (The bright, square parts of the uncompressed submatrices are due to two points being on the same vertical edge, of which the geometry has four.)

We first compute the entire matrix for wavenumber $\nu = 2$, see Figures 3 (a) and 4 (a). The matrices are compressed by discarding (*a posteriori*) elements smaller than a certain threshold, which here is chosen as $\varepsilon_{\text{cubic}} = 0{\cdot}1$ for the cubic case, and $\varepsilon_{\text{linear}} = 0{\cdot}2$ for the linear case, see Figures 3 (b) and 4 (b), respectively. We observe significant compression for both the linear and cubic spline bases. From this the compression mask is defined. We then perform compression of the corresponding matrices for different wavenumbers, namely $\nu = 0$ and $\nu = 1$ using the defined compression mask. The result is shown in Figures 3 (c-d) and 4 (c-d). We also perform *a posteriori* compression for $\nu = 0$ and $\nu = 1$ with the same thresholds $\varepsilon_{\text{cubic}} = 0{\cdot}1$ and $\varepsilon_{\text{linear}} = 0{\cdot}2$, and find that no additional elements are discarded by the *a priori* compression. Further discussion of the use of the different bases is given in Section 6.

It is of interest to estimate the number of matrix elements retained after compression. We proceed as follows: Assume that the geometry has a number of $\mathcal{C}$ corners (here we have four corners). Furthermore we assume that the finest space is V_J, that the wavelets have support of length m and have N vanishing moments. For all wavelet coefficients which have no singularity in their support, *i.e.*, there is no corner for any t in the support of $\tilde{\psi}^j_k(t)$ or u in the support of $\phi^j_l(u)$, assume that N is so large that $\varepsilon_{j,k,l} < \hat{\varepsilon}$ for these coefficients. Then, the number of remaining wavelet coefficients will be less than or equal to ($\mathcal{C}$ corners, 3 wavelet submatrices, 2 strips of $2^j \cdot m$ coefficients for each singularity, levels $j = 0, \ldots, J-1$)

$$\sum_{j=0}^{J-1} \mathcal{C} \cdot 3 \cdot 2(2^j \cdot m) = \text{const.} \cdot m \cdot (2^J - 1) \;\leq\; \text{const.} \cdot m \cdot n \tag{47}$$

where $n = 2^J$ is the number of unknowns for an uncompressed system. For wavelets with sufficiently many vanishing moments, we see that the number of retained elements is $\mathcal{O}(n)$.

We note that in practice most of the elements of the strips of size $2^j \cdot m$, $j = 0, \ldots, J-1$, in our compression strategy are discarded, thus making the number of retained matrix elements smaller than estimated in (47). This is because these elements are smaller than the given threshold even if $\bar{K}$ is not smooth on the support of the corresponding wavelets.

With the compression strategy we can use a moderate N and thus a moderate m, while still retaining a high accuracy of the computations and a high compression rate of the matrix.

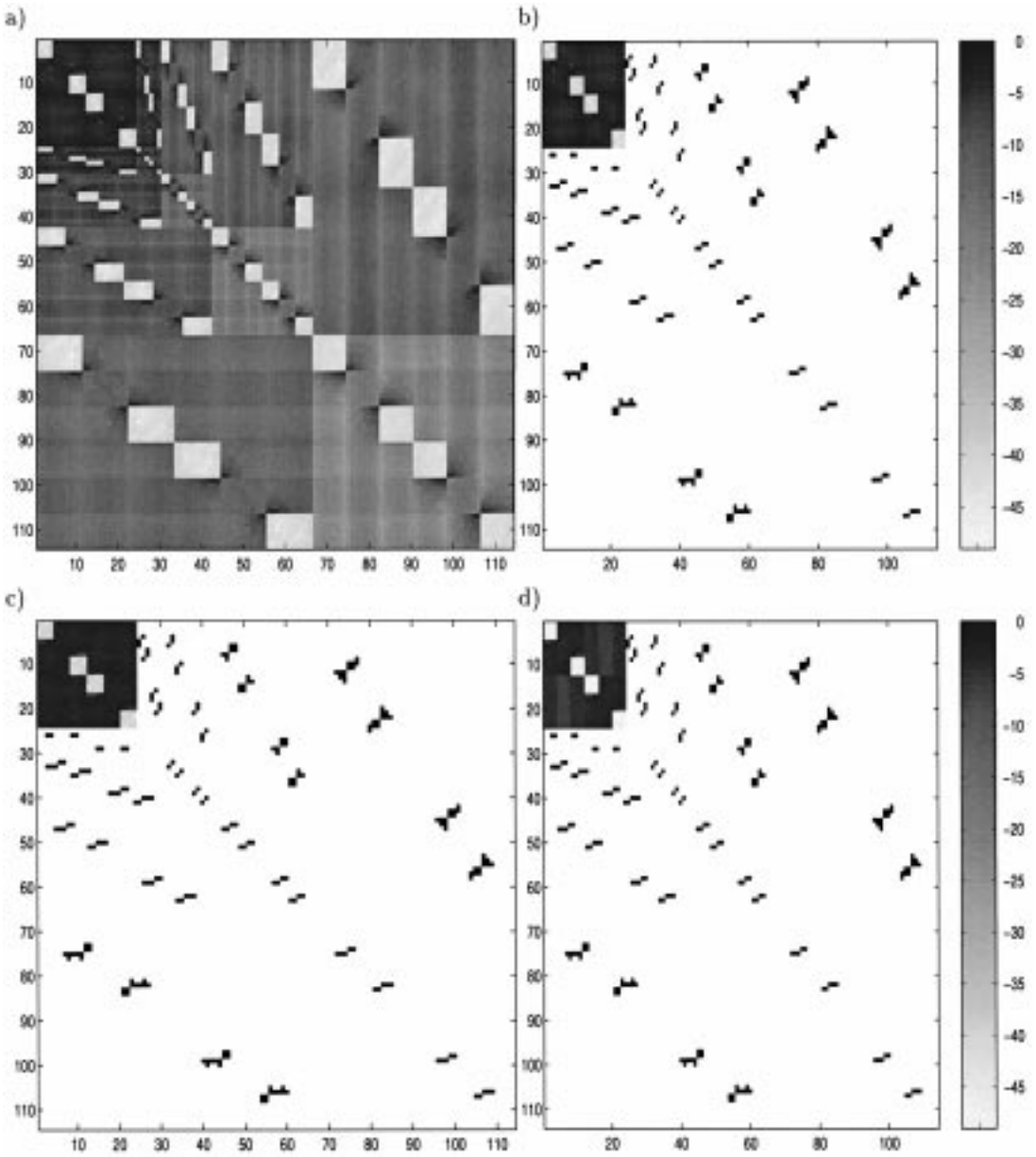

Figure 3. Cubic spline wavelet basis. The matrix before compression (a), the elements retained after compression with $\varepsilon = 0{\cdot}1$ and $\nu = 2$ (b), the elements retained after compression for $\nu = 1$ and the same compression mask (c) and for $\nu = 0$ and again the same compression mask (d). Geometry B (Figure 5).

6. Computation of wave properties and hydrodynamic forces

We now apply the method to compute hydrodynamic forces and reflection properties of a single or multiple rectangular cylinders which are floating in the free surface, see Figure 5. Geometry A (a single rectangular cylinder) is chosen because of its simplicity, and for this geometry we also have available an analytical solution for the sway problem when the wavenumber $\nu \to 0$. Geometries B and C are relevant for a sectionwise investigation of a

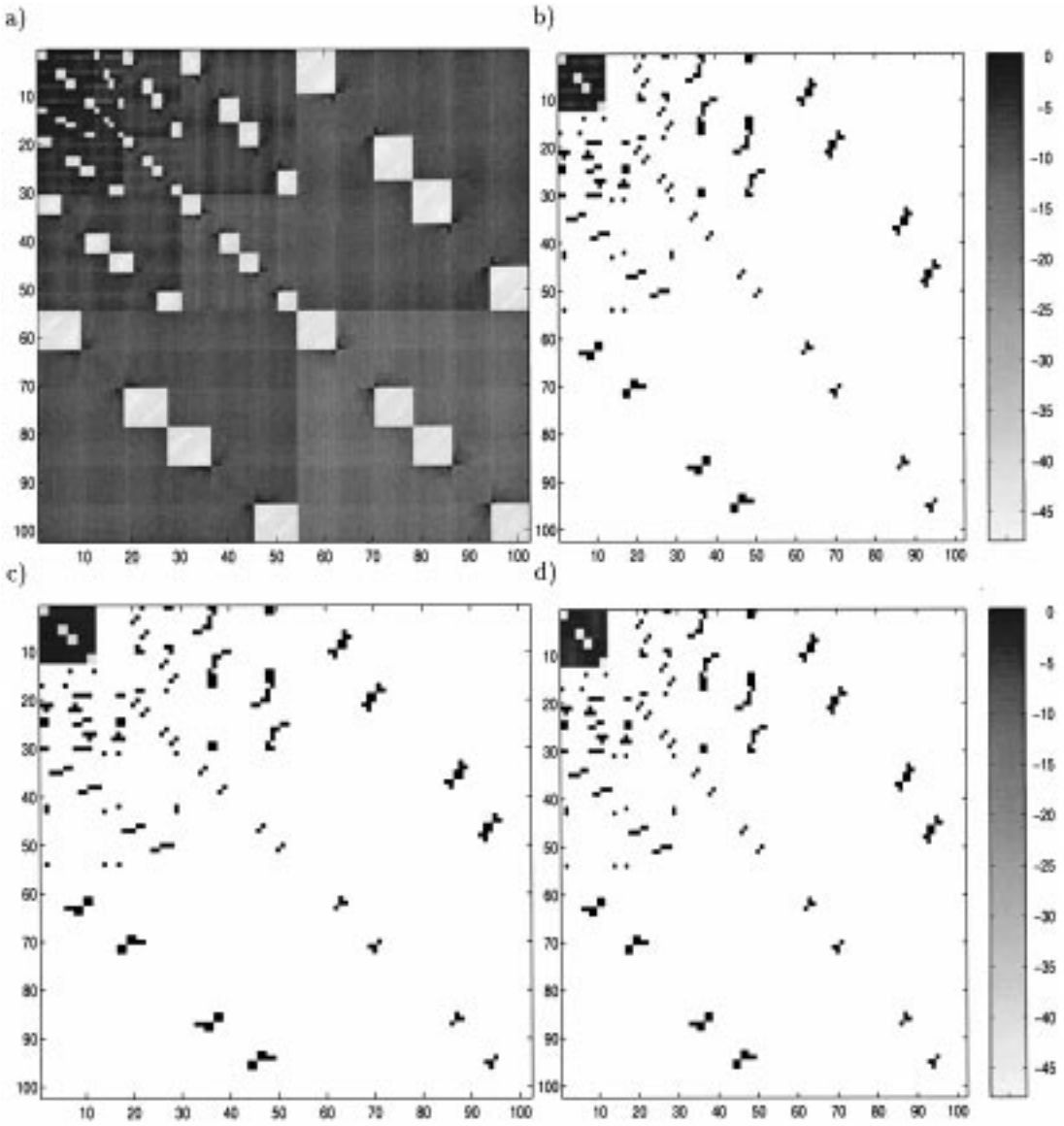

Figure 4. Same as Figure 3, but linear spline wavelet basis and $\varepsilon = 0{\cdot}2$.

catamaran, in the context of application of strip theory. Geometry D is chosen because we want to investigate the performance of the method for an N-body problem, with large N. (The latter geometry may be relevant for hydrodynamic analysis of large floating or anchored structures like, *e.g.*, an airport.)

We consider both the radiation and the diffraction problem. In the radiation problem (see Equations 12 and 17) we compute the added mass and damping coefficients in sway and heave, *i.e.*, (a_{11}, b_{11}) and (a_{22}, b_{22}), which are defined by

$$\omega^2 a_{ij} - \mathrm{i}\omega b_{ij} = -\mathrm{i}\omega\rho \int_{S_B} \hat{\chi}_j n_i \, \mathrm{d}S. \tag{48}$$

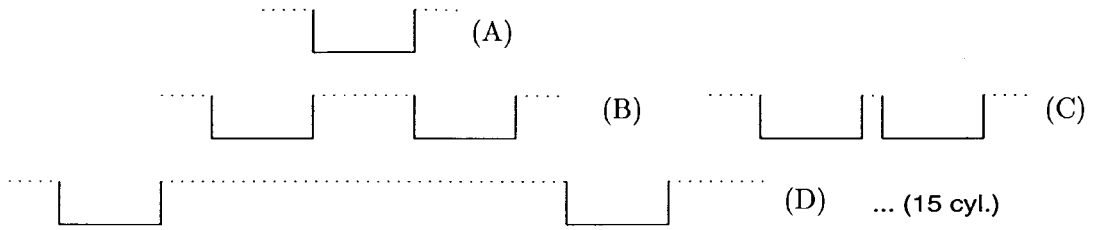

Figure 5. Geometries, henceforth referred to as geometry A to D. All cylinders are twice as wide (beam $2T_0$) as deep (draught T_0), and the distance between the center of two adjacent cylinders is $4T_0$ for geometry B, $12T_0/5$ for geometry C and $40T_0$ for geometry D.

In the diffraction problem (see equations 13 and 17) we compute the reflection coefficient R, where

$$\hat{\chi}_7 \to R\mathrm{e}^{\mathrm{i}\nu x+\nu y} \tag{49}$$

as $x \to -\infty$, and the transmission coefficient T, where

$$\hat{\chi}_7 \to (T-1)\mathrm{e}^{-\mathrm{i}\nu x+\nu y} = (T-1)\hat{\chi}_0 \tag{50}$$

as $x \to \infty$, and also the horizontal exciting force X_1, determined by

$$X_1 = -\rho \int_{S_B} (\hat{\chi}_0 + \hat{\chi}_7) n_i \, \mathrm{d}S \tag{51}$$

Conservation of energy gives that $|R|^2 + |T|^2 = 1$, which provides a check of the computations.

6.1. Comparison of different bases – added mass and damping coefficients

First, we compare application of the different bases; linear spline wavelets, cubic spline wavelets and Daubechies wavelets. In Figure 6, a_{11} and b_{11} for geometry A in the sway mode of motion are shown for selected wavenumbers $0 < \nu < 1{\cdot}5$. In addition to the solution of the uncompressed systems, solutions for compression with different thresholds are shown. These thresholds are chosen to highlight the differences between the bases when subjected to massive compression. The compression error depends on both the threshold and the wavelet basis, so the thresholds are selected to get comparable compression ratios for the different bases, when possible. We may then compare the errors. We plot the results for the linear spline wavelet basis with compression thresholds $\varepsilon_{\text{lin.,}\,1} = 0{\cdot}1$ and $\varepsilon_{\text{lin.,}\,2} = 0{\cdot}6$, the cubic basis with compression thresholds $\varepsilon_{\text{cubic,}\,1} = 0{\cdot}12$ and $\varepsilon_{\text{cubic,}\,2} = 10$ and the Daubechies basis with compression threshold $\varepsilon_{\text{Daub.,}\,1} = \varepsilon_{\text{Daub.,}\,2} = 100$. (The latter large compression thresholds mean that the compression ratio is still less than for the other bases.)

From Figure 6, we see that only the linear basis (Figure 6 a) gives a visibly less accurate result than the other two bases. The linear basis has fewer vanishing moments than the other two, and its scaling functions are less smooth than those of the cubic spline basis. Figure 6 (c) shows that the Daubechies basis gives a more accurate result than the linear spline basis.

However, a direct comparison like this with the Daubechies basis is made difficult because the interval-adaption of the Daubechies basis forces us to use at least N scaling *end*-functions. This means that the coarsest level for $N = 3$ will be $J = 3$, giving 8 scaling functions, compared to the linear spline basis, where we have only 3 scaling functions on the coarsest level.

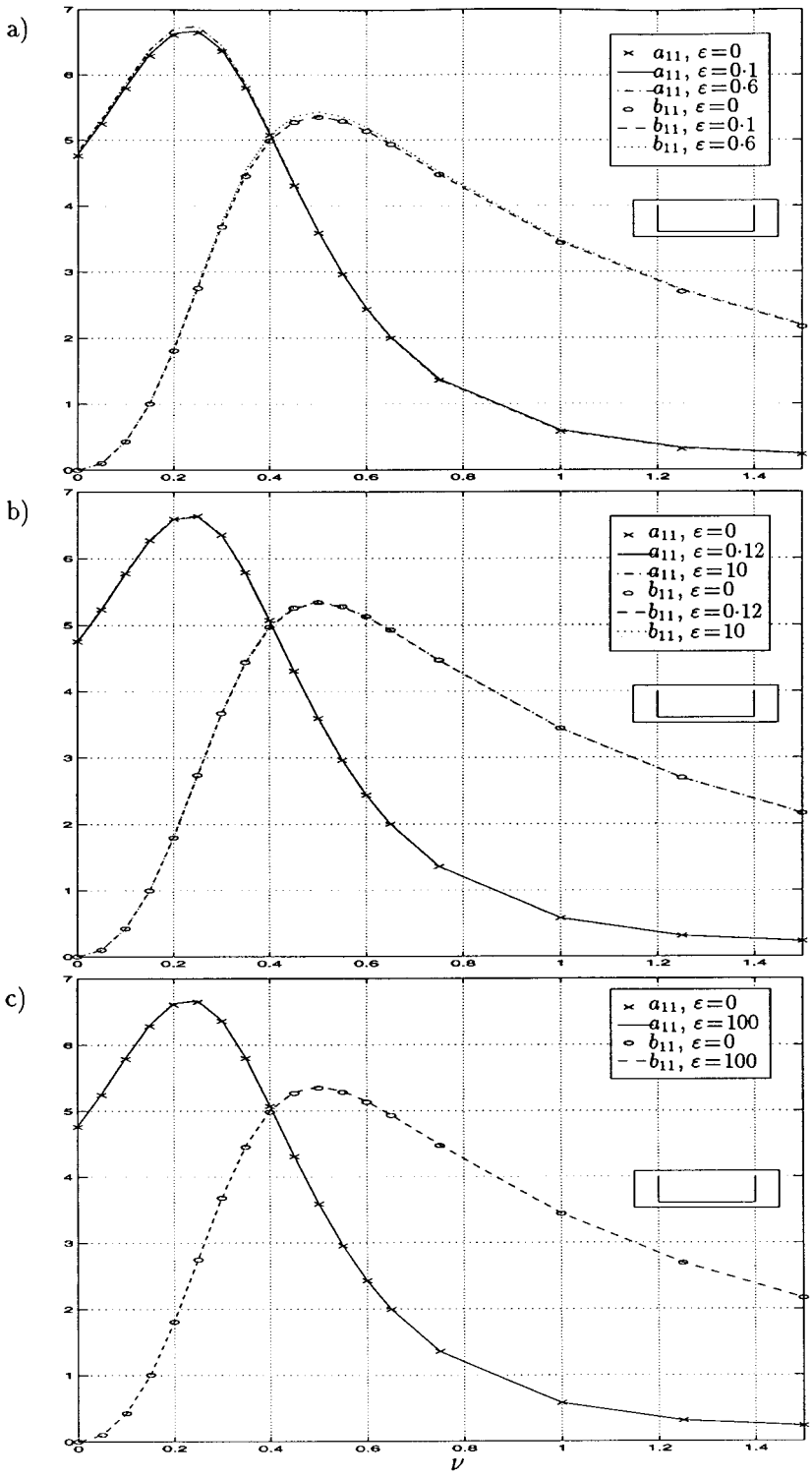

Figure 6. Comparison of linear spline wavelets (a), cubic spline wavelets (b), and Daubechies wavelets (c). Added mass a_{11}, normalized by ρT_0^2, and damping coefficients b_{11}, normalized by $\rho T_0^2 \omega$, for geometry A. Crosses and rings: no compression. Solid and dashed lines: *a priori* compression with compression threshold $\varepsilon_{\cdot,1}$. Dash-dotted and dotted lines: *a priori* compression with compression threshold $\varepsilon_{\cdot,2}$.

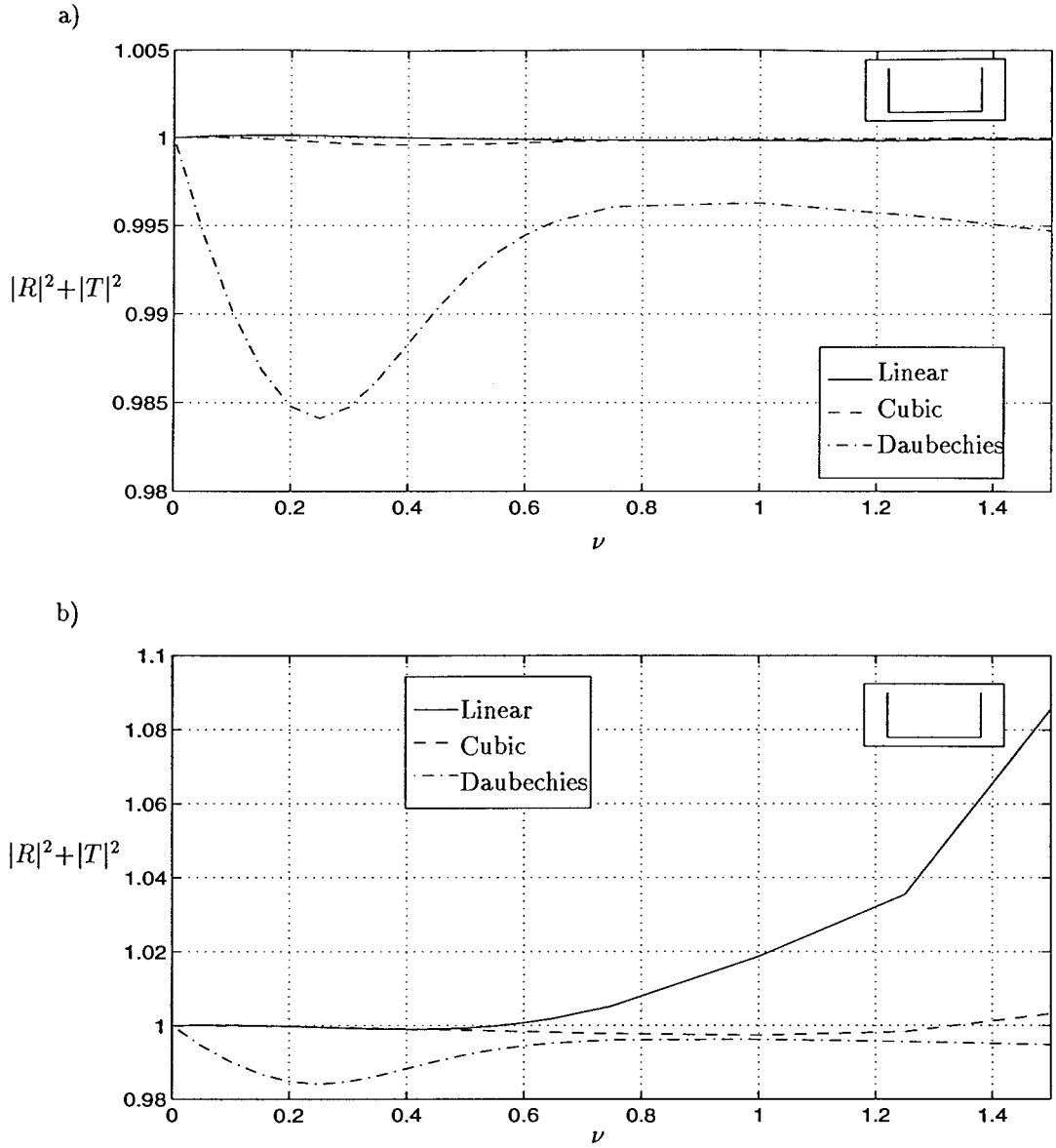

Figure 7. $|R|^2 + |T|^2$ for geometry A. Comparison of linear spline wavelets (solid line), cubic spline wavelets (dashed line), and Daubechies wavelets (dash-dotted line). Without compression (a) and with *a priori* compression (b). Compression masks were determined for $\nu = 1{\cdot}5$, and $\varepsilon_{\text{lin.,1}} = 0{\cdot}1$, $\varepsilon_{\text{cubic,1}} = 0{\cdot}12$, and $\varepsilon_{\text{Daub.,1}} = 100$, as in Figure 6.

Also, non-normalisation of the end-wavelets excludes these from the compression. The effect is that coarse discretizations, even combined with large thresholds, lead to less compression than for the spline wavelet bases.

In Figure 7 we have graphed $|R|^2 + |T|^2$ for geometry A, without compression (a) and compressed with thresholds $\varepsilon_{\text{lin.,1}} = 0{\cdot}1$, $\varepsilon_{\text{cubic,1}} = 0{\cdot}12$, and $\varepsilon_{\text{Daub.,1}} = 100$, as in Figure 6, and compression masks determined for $\nu = 1{\cdot}5$ in (b). Without any discretization or numerical error, we have that $|R|^2 + |T|^2 = 1$, so we see that the proposed method do not conserve

the energy perfectly. The number of discarded matrix elements is almost the same for the linear and cubic bases, and from Figure 7 (b) we see that the cubic basis is the most accurate of the two. Since the compression mask was determined for $\nu = 1{\cdot}5$, and the kernel gets smoother for smaller ν, we expect the compression mask to yield better results for smaller wavenumbers, as observed in the figure, since the significance of the discarded coefficients decreases. The Daubechies basis starts out better for the higher wavenumbers because of a smaller compression rate, as commented on above. For the smaller wavenumbers, since the significance of the discarded coefficients decreases, we approach a situation like the one in (a), where the spline wavelets, and particularly the cubic one, performs better. One of the reasons for this is believed to be the lesser smoothness of the Daubechies basis as compared to the spline wavelet bases.

6.2. Computations with cubic spline wavelets and different thresholds

For geometry A, B and C, we have solved equation (12) and (13) for the heave problem, and the added mass coefficient a_{22} and the damping coefficient b_{22} are depicted in Figure 8 and 9 (a). The computations are performed with the cubic basis and $J = 4$. When compressing with threshold $\varepsilon = 0{\cdot}1$, 96·7% of the matrix for geometry A is discarded, and 97·7% for geometry B. This corresponds to retaining approximately $19{\cdot}1^2$ and 16^2 elements per cylinder, respectively. When using the threshold $\varepsilon = 0{\cdot}02$, 95·0% and 96·9% will be compressed, giving approximately $23{\cdot}5^2$ and $18{\cdot}6^2$ elements per cylinder. For geometry B we get a moderate physical resonance for wavenumbers around $\nu \approx 0{\cdot}24$. At this resonance, we see that a minor error in the added mass coefficient due to the compression becomes visible.

For geometry C, we get a strong physical resonance effect at $\nu \approx 0{\cdot}675$. This geometry was chosen for the purpose of comparison (not shown here) with 3d computations by Newman and Sclavounos [15] for a catamaran, using a low-order panel method. Compression with thresholds $\varepsilon = 0{\cdot}02$ and $\varepsilon = 0{\cdot}1$, give compression ratios 96·7% and 97·7%, *i.e.*, $19{\cdot}1^2$ and $15{\cdot}9^2$ matrix elements per cylinder. We notice that the computed resonance frequency differs slightly from the correct one when the compression is too strong. We see the same effect in the plots of the reflection and transmission coefficients, Figure 9 (b). In Figure 9 (c) we see that also $|R|^2 + |T|^2$ will differ from 1 around the resonant frequency.

6.3. A row of cylinders

A more involved case is geometry D. For this geometry, we want to examine the compression scheme in computing the forces on the individual cylinders. We can also make qualitative comparisons with the results in 3 dimensions by Maniar and Newman [5].

In Figure 10 we show the hydrodynamic forces and the reflection/transmission properties for the array of cylinders, using cubic spline wavelets. The wavenumbers are chosen close to the smallest resonant wavenumber, approximately at $\nu = 2\pi/(2L) \approx 0{\cdot}31$. We note that some inaccuracies occur at the physical resonance, where *e.g.*, $|R|^2 + |T|^2$ does not quite add up to one.

If we compute the force component $|X_1^j|$ on each of the cylinders $j = 1, \ldots, 15$, and normalize with respect to $|X_1|$ for a single cylinder, we would expect the force to be largest for the cylinder(s) at the resonant wavenumber. We can see that this in fact happens for $\nu = 0{\cdot}28296$, where the maximal force on cylinder number 8 is about 8 times that for one isolated cylinder, Figure 10 (c). The results show that a significant relative error in the load distribution on the individual cylinders can only be detected for a high compression rate, and only in the

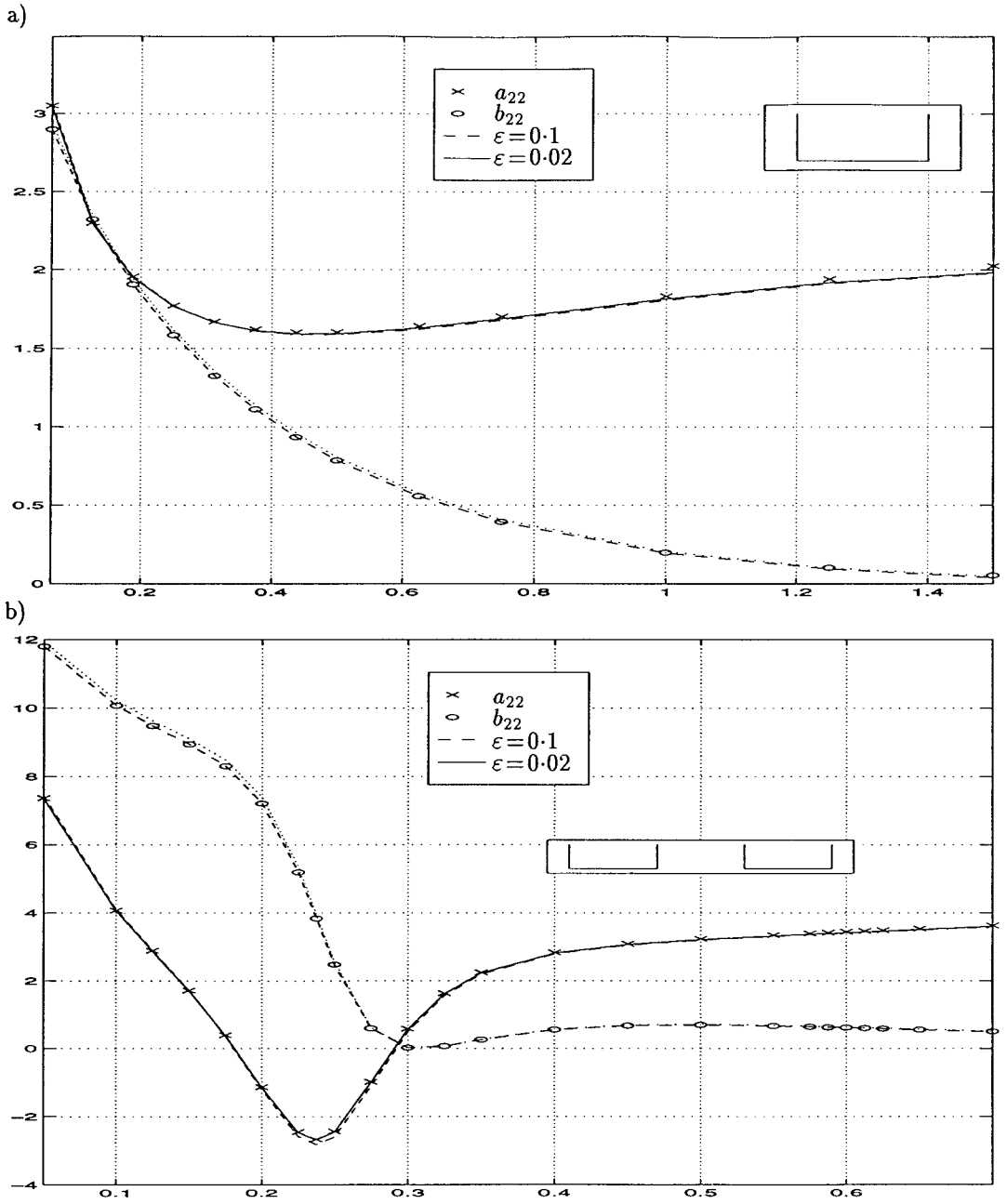

Figure 8. Added mass a_{22}, normalized by ρT_0^2, and damping coefficients b_{22}, normalized by $\rho T_0^2 \omega$, for geometry A (a) and geometry B (b). Crosses and rings: no compression. Solid lines: *a priori* compression with compression threshold $\varepsilon = 0{\cdot}02$. Dashed lines: *a priori* compression with compression threshold $\varepsilon = 0{\cdot}1$. Cubic basis, $J = 4$.

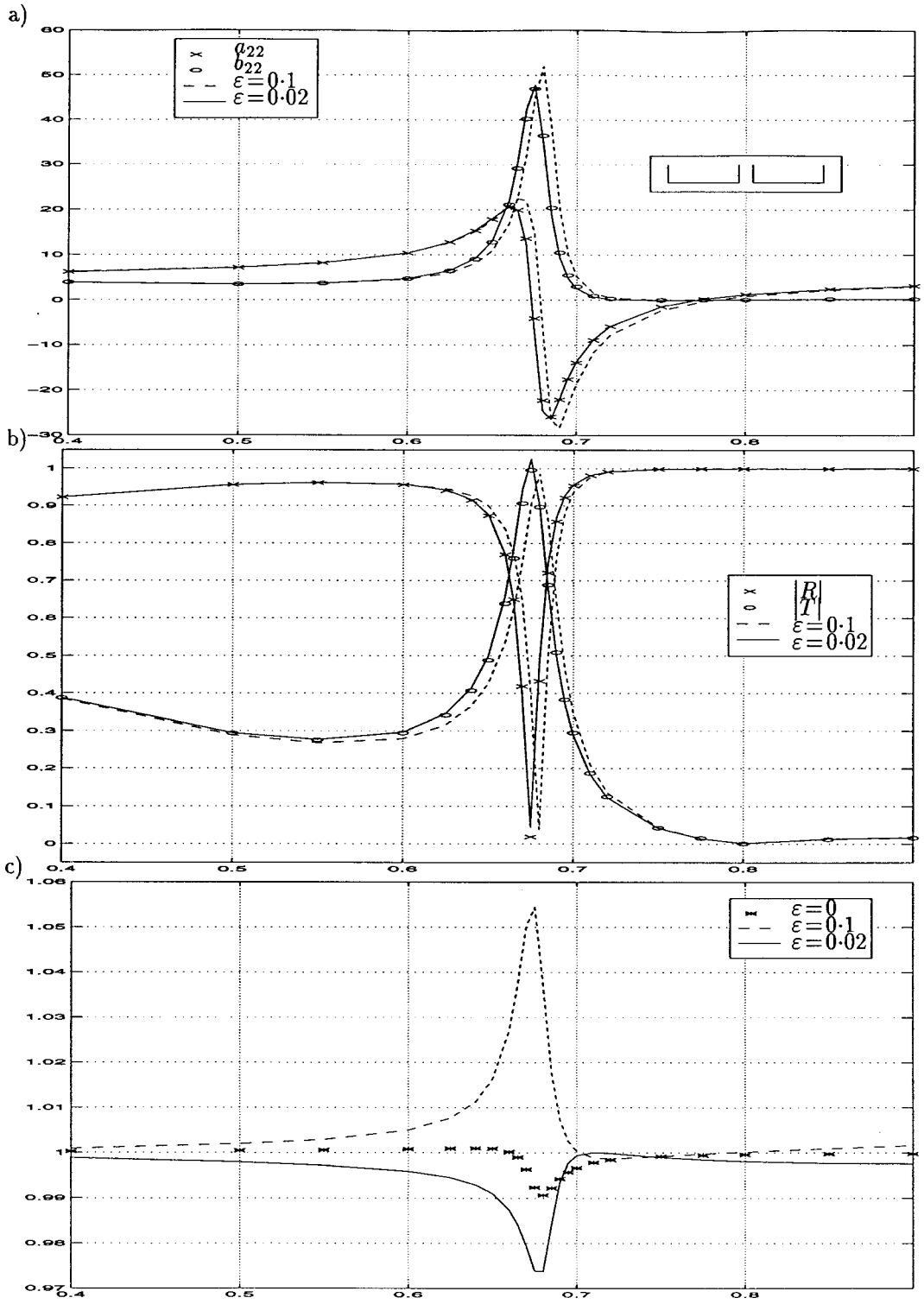

Figure 9. Added mass a_{22}, normalized by ρT_0^2, and damping coefficients b_{22}, normalized by $\rho T_0^2 \omega$ (a). $|R|$ and $|T|$ (b), and $|R|^2 + |T|^2$ (c). Crosses and rings: no compression. Solid lines: *a priori* compression with compression threshold $\varepsilon = 0{\cdot}02$. Dashed lines: *a priori* compression with compression threshold $\varepsilon = 0{\cdot}1$. Cubic basis, $J = 4$, geometry C.

close vicinity of the resonant wavenumber. For the cylinder with the highest load, the relative error due to the compression is then about 10% for threshold $\varepsilon = 0{\cdot}1$ and compression ratio 98·56% (corresponding to $12{\cdot}6^2$ retained matrix elements per cylinder.) For $\varepsilon = 0{\cdot}01$ and compression ratio 98·37% (corresponding to $13{\cdot}4^2$ retained matrix elements per cylinder) the relative error is less than 1%. Overall, we get good accuracy with high compression.

We see that the compression introduces a minor shift of the resonant frequency, as illustrated in Figures 10 (a) and (b). The shift appears as an error in the force on the cylinders for the frequencies just below and above the resonant one, see Figure 10 (c).

6.4. Local property near a corner for $\nu \to 0$

Finally, we study geometry A in the sway mode of motion for $\nu = 0$ *i.e.*, effectively unit speed in the horizontal direction. The potential χ, which is a solution of equation (12) or (13), is singular at the corners, and behaves there as $\chi \sim s^{2/3}$ for $s \to 0$, where s is the distance from the corner. An analytical solution (in terms of elliptic integrals) by the method of Schwarz-Christoffel transformations is available for this problem, see Appendix C.

In Figure 11, solutions due to uncompressed systems with a finest resolution corresponding to $J = 4$, $J = 5$ and $J = 6$ for the cubic spline wavelet basis are shown. The potential χ is graphed against the distance s from the corner in double-logarithmic plots, where the slope of the exact potential becomes $2/3$ for $s \to 0$. Together with this is also shown the solution obtained by the Schwarz-Christoffel transformation. Since the systems are uncompressed, there are $2^{J+1} + 3$ uniformly spaced basis functions on each edge, giving 105^2, 201^2 and 393^2 matrix elements, respectively.

In Figure 12 the system for $J = 6$ is compressed with thresholds $\varepsilon = 0{\cdot}02$ and $\varepsilon = 0{\cdot}1$, as before. This reduces the number of matrix elements to approximately 36^2 and 27^2, respectively. The accuracy is not significantly reduced due to the compression. From this we conclude that the matrix elements discarded are those corresponding to basis functions with support far away from the corners.

6.5. Geometry without corners

We have seen that corners in the geometry causes the matrix of wavelet coefficients to contain regions with large coefficients, due to the parameter values for the corners being in, or close to, the supports of the integrals for the coeffcients. After compression, the small elements will be discarded while the large ones remain. For a geometry without corners we do not get all these large coefficients. This means that we can get high compression rates, but it also means that we might have chosen a much coarser discretization in the first place. This is a case where the wavelet method is not really needed, but it will of course work just as well.

In Figure 13 (b), we have extracted the submatrix D_3^d of Eq. (46) for geometry B, see Figure 3 (a), and in Figure 13 (c) the corresponding submatrix of level 5 of a half-immersed circular cylinder as depicted in (a) is shown. We see clearly that the large wavelet coefficients due to the corners in Figure 13 (b) do not appear to have a counterpart in Figure 13 (c). The latter does have some areas of larger coefficients, although far less significant than for the square cylinders, which are due not to corners, but rather to the joinings of polynomial pieces in the spline used to approximate the semicircle.

When compressed with thresholds chosen to produce the same relative error in integrated values, like *e.g.*, added mass, the wavelet coefficients for the spherical cylinder are all dis-

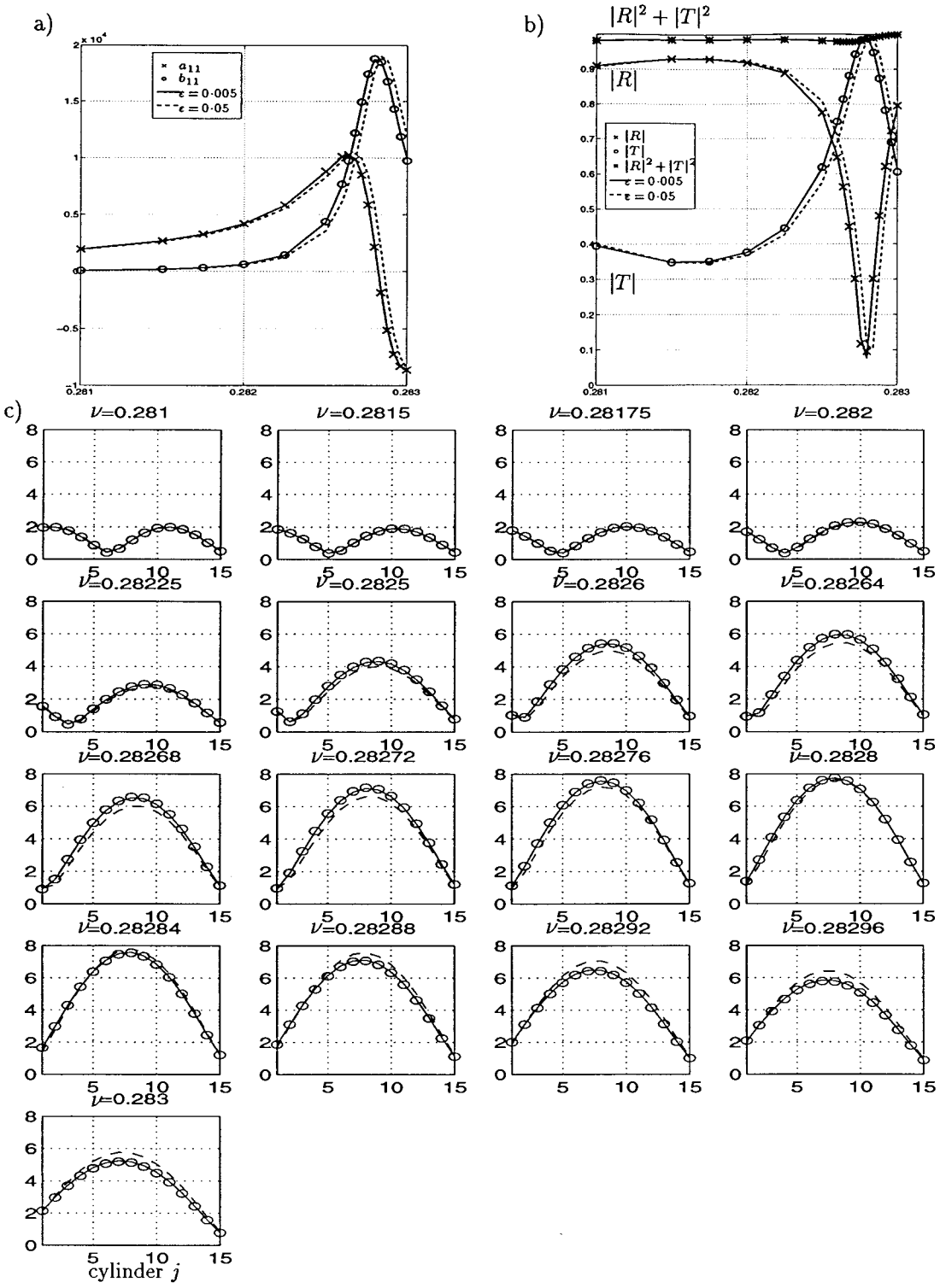

Figure 10. Added mass a_{11}, normalized by ρT_0^2, and damping coefficients b_{11}, normalized by $\rho T_0^2 \omega$ (a). $|R|$, $|T|$ and $|R|^2 + |T|^2$ (b). The force component $|X_1^j|$ normalized with respect to $|X_1|$ for a single cylinder, (vertical axis), vs. cylinder number j, $j = 1, \ldots, 15$ (horizontal axis). Wavenumbers $0{\cdot}281 \leq \nu \leq 0{\cdot}283$ (c). Crosses and rings: no compression. Solid lines: *a priori* compression with compression threshold $\varepsilon = 0{\cdot}005$. Dashed lines: *a priori* compression with compression threshold $\varepsilon = 0{\cdot}05$. Cubic basis, $J = 4$, geometry D.

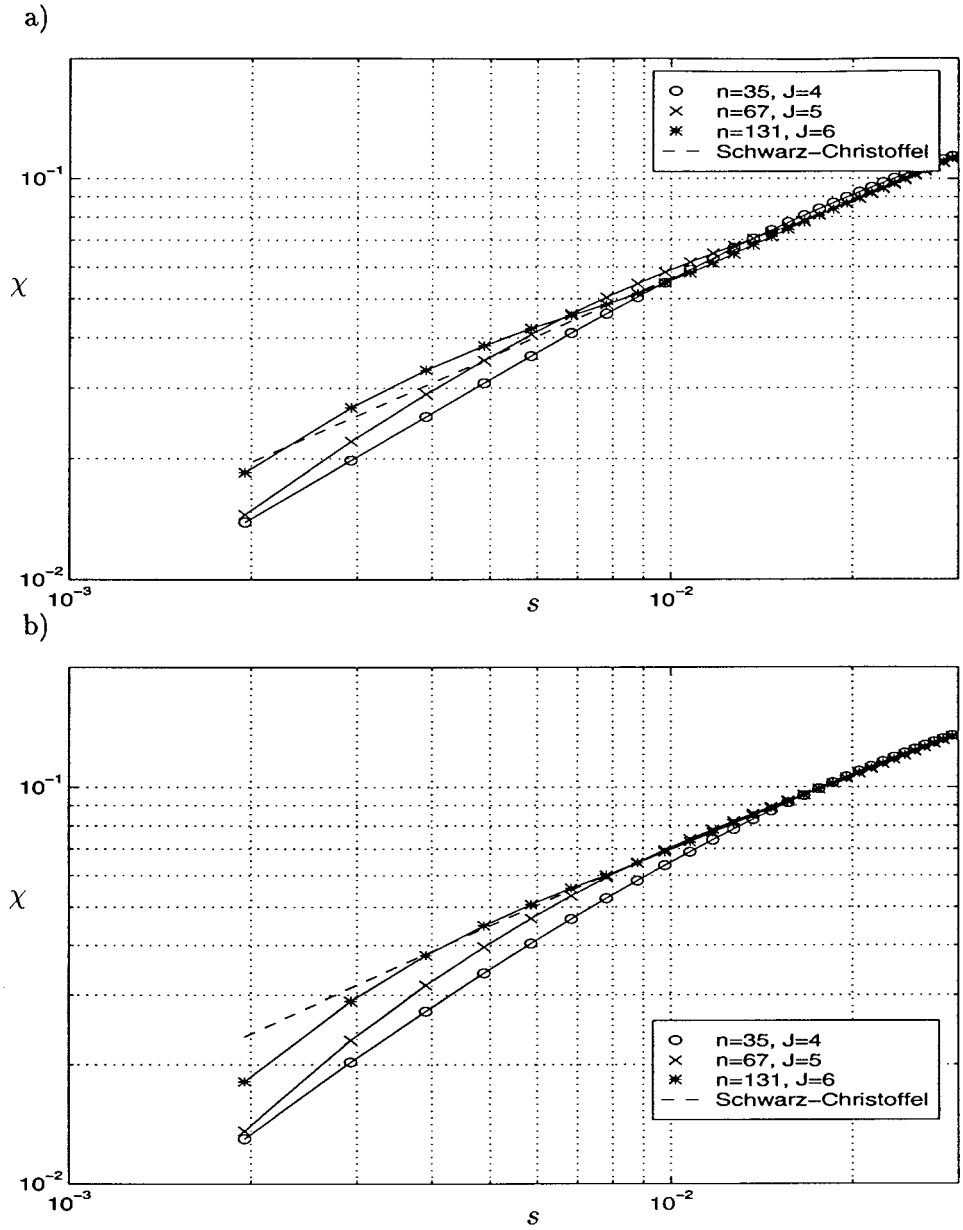

Figure 11. The potential for $\nu = 0$, sway mode of motion, near the corners of geometry A. The potential along the vertical edge (a) and the horizontal edge (b), with the distance from the corner along the abscissas. The dashed line corresponds to the Schwarz-Christoffel solution, see Appendix C. The number n ($n = 35$, $n = 67$, $n = 131$) of basis functions along each edge is indicated. Cubic spline wavelet basis, no compression, three choices of finest space V_J, $J = 4, 5, 6$.

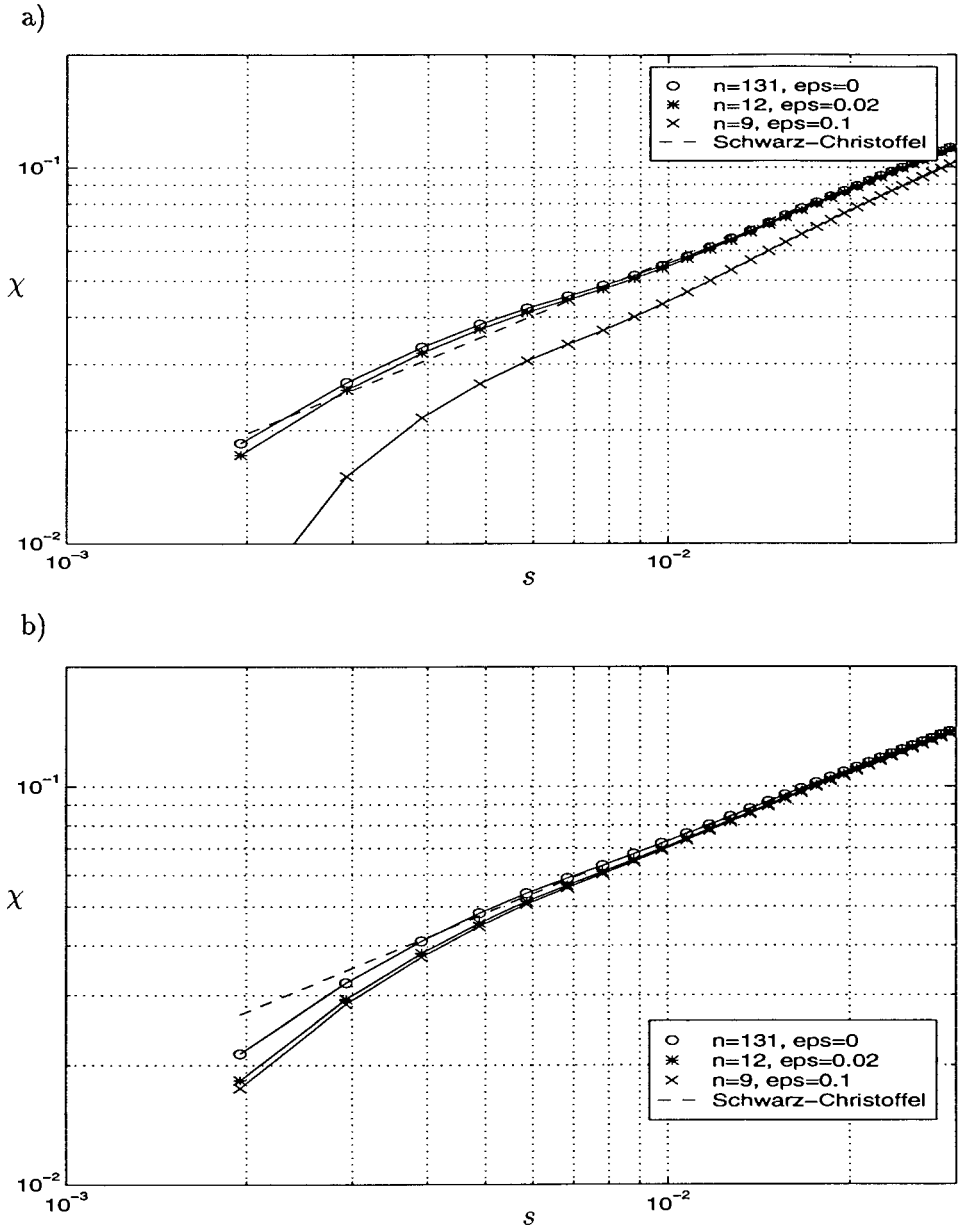

Figure 12. As in Figure 11, but with compression. The number n shown in the figures is the square root of the number of non-zero matrix elements for each edge after compression. Thresholds are $\varepsilon = 0{\cdot}02$ (giving $n = 12$) and $\varepsilon = 0{\cdot}1$ (giving $n = 9$).

carded, meaning that we get enough accuracy by using just the scaling functions at the coarsest level.

7. Conclusions

We have applied wavelets, in the form of a multiresolution analysis, for the solution of a Fredholm integral equation of the second kind that arises in wave analysis of floating bodies.

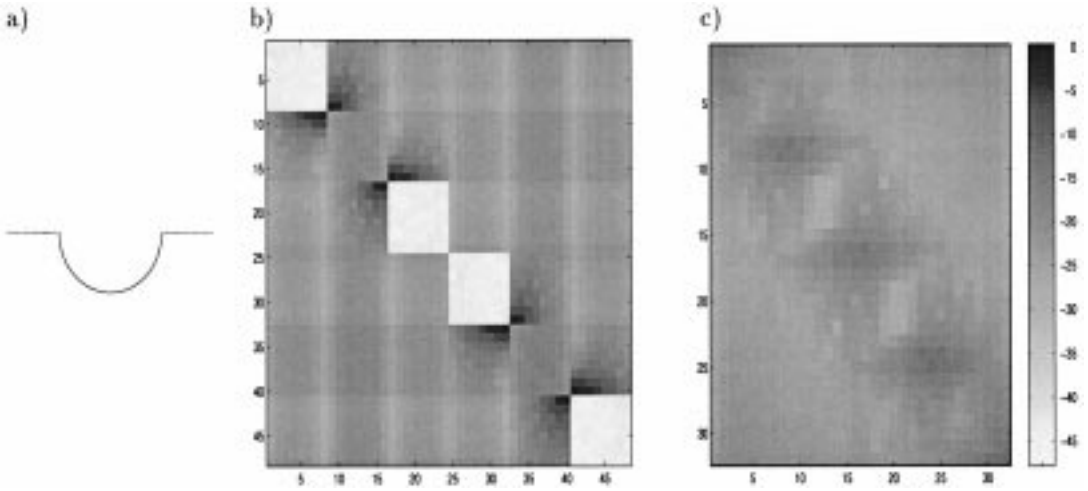

Figure 13. Depicted is a circular cylinder (a) and accompanying wavelet coefficients D_5^d (c). Also, corresponding coefficients (D_3^d) from Figure 3 (a) are shown for comparison (b). The basis is the cubic spline basis, and the wavenumber is $\nu = 0$.

The kernel of the integral equation, together with the unknown potential and the right-hand side of the equation, is expanded in wavelet bases. A linear system with a highly compressible matrix is thus obtained. The linear system is well conditioned, so the computational load of solving it is proportional to the number of non-zero matrix elements. We have seen which matrix elements can be discarded, and for what kind of geometries this method will be advantageous, namely for geometries with corners. For a kernel without such singularities, *i.e.*, resulting from a smooth geometry, the method still works. In this case, however, we could choose a coarser discretization instead of choosing a fine and uniform discretization followed by compression. We would still have the nice property of biorthogonality offered by the biorthogonal spline scaling functions.

Differences between a coarse and fine approximation are represented in terms of the wavelets, and the compressibility of the matrix is due to the vanishing moments of these wavelets. The maximal compression rate of the linear system has been estimated, and it is found that for wavelets with a sufficiently large number of vanishing moments, the wavelet method will give an $\mathcal{O}(n)$ algorithm, where n is the initial number of (scaling and wavelet) functions in which the solution is expanded. A practical *a priori* compression scheme utilising thresholding and a common compression mask for several wavenumbers has been developed and shown to work well for selected geometries.

Two kinds of wavelets have been investigated for this purpose, biorthogonal spline wavelets and Daubechies wavelets. The Daubechies wavelets were found not to be very well suited to problems involving a large number of small intervals, but it was found that biorthogonal spline wavelets, in particular cubic ones, are very well suited with respect to accuracy and efficiency.

The method has been applied to arrays of rectangular cylinders. Among others, we have considered an array of 15 rectangular cylinders. Sufficient accuracy has been achieved with a high compression ratio in the computation of various hydrodynamic forces and reflection/transmission properties. The chosen problems also exhibit resonant behaviour, and the method is performing satisfactorily also in these cases. A more detailed look at the local prop-

erties near a corner confirms that the compression removes redundancy far from the corner, without degrading the solution close to the corner.

It is clear that the method will be well suited for complicated and/or large geometries, in particular where the choosing of trial functions is difficult. In these cases, the compression will remove redundancy in the initially uniformly distributed trial functions. We will in effect get an adaptive method with different resolutions, low resolution where the geometry/solution is smooth, and high resolution where the geometry/solution is less well-behaved.

We believe that the need for solving continuously larger and more complicated problems, with ever more accuracy, will drive the continued development of adaptive wavelet methods, and also other adaptive methods. The method here described, based on the biorthogonal spline wavelets of Mørken and Nygaard [6] is promising. The use of these wavelets can be regarded as an extension of the use of B-splines. Where approximation spaces spanned by B-splines have been used, new coarser and finer spaces can easily be introduced, and then the biorthogonal spline wavelets are just the basis functions spanning the differences between the original B-spline approximation and the coarser/finer approximations.

Among the interesting extensions of the method discussed in this work, would be *e.g.*, the extension to three dimensions, non-uniform knots of the spline wavelets and improvement of *a priori* compression schemes.

The extension to three dimensions does introduce some new problems, but not of an intractable nature. If the geometry can be modelled by a set of two-dimensional tensor-product spline patches, we may also use two-dimensional tensor-products for the expansion of the solution of the integral equation. The kernel will then have to be expressed in four-dimensional tensor products of the scaling and wavelet functions, resulting in one new scaling function and 15 wavelets. The actual computation of the wavelet coefficients will also be more critical, due to the quadruple integrals involved. With respect to the implementation process, the mere bookkeeping needed will demand some effort. In three dimensions we also get richer behaviour in the geometry. We do not only have corners, but corners of different kinds and also edges, which will cause large wavelet coefficients. One will also have to treat degenerate cases of patches, *e.g.*, rectangular patches with collapsing edges. In spite of these technical challenges, we expect that (spline) wavelet methods for the solution of wave-body problems in three dimensions will make it possible to set up even sparser systems than was done here in two dimensions, without compromising the accuracy.

Acknowledgement

This research was funded by the Research Council of Norway through the ‘Toolkits in Industrial Mathematics’ programme.

Appendix A. Multiresolution analysis

As seen in Section 3, the multiresolution analysis can be regarded as set of nested spaces with bases which decomposes functions with respect to different frequencies, much like a decomposition into harmonic functions. One advantage of wavelets is that they are *local in space*, as opposed to the harmonic functions.

A multiresolution analysis of $L^2(\mathbb{R})$ is more precisely defined as a sequence of closed approximation spaces $V_j \subset \mathbb{R}$, $j \in \mathbb{Z}$, such that

1. $V_j \subset V_{j+1}$,
2. $v(x) \in V_j \Leftrightarrow v(2x) \in V_{j+1}$,
3. $v(x) \in V_0 \Leftrightarrow v(x+k) \in V_j$ for all $k \in \mathbb{Z}$,
4. $\bigcup_{j=-\infty}^{\infty} V_j$ is dense in $L^2(\mathbb{R})$,
5. $\bigcap_{j=-\infty}^{\infty} V_j = \{0\}$,

and finally, there must be a *scaling function* $\phi \in V_0$ with a non-vanishing integral such that the set $\{\phi(x-k)\}$ for all $k \in \mathbb{Z}$ is a Riesz basis of V_0. (See *e.g.*, Jawerth and Sweldens [10] or Daubechies [9], the latter has a definition of the Riesz basis, pp. xviii—xix.)

Let W_j be a complementary subspace to V_j in V_{j+1}, $V_j + W_j = V_{j+1}$, *i.e.*, all $u \in V_{j+1}$ is a sum of unique $v \in V_j$ and $w \in W_j$. The multiresolution analysis is constructed so that there is a Riesz basis $\{\psi(t-k)\}_{k\in\mathbb{Z}}$ for W_0. The function ψ is the *mother wavelet*. It then follows that $g(t) \in W_j$ if and only if $g(2t) \in W_{j+1}$. This construction implies that for a given j, the functions ϕ_k^j and ψ_k^j, given in (20) and (21), constitute Riesz bases for the spaces V_j and W_j, respectively. This is valid for all j, k.

If we denote the projection operator from V_{j+1} to V_j by P_j, and the projection operator from V_{j+1} to W_j by Q_j, we can depict the multiresolution analysis like this:

$$
\begin{array}{ccccccccc}
V_j & \underset{P_j}{\rightarrow} & V_{j-1} & \cdots & \underset{P_2}{\rightarrow} & V_1 & \underset{P_1}{\rightarrow} & V_0 \\
 & \underset{Q_j}{\searrow} & & & \underset{Q_2}{\searrow} & & \underset{Q_1}{\searrow} & \\
 & & W_{j-1} & & & W_1 & & W_0
\end{array}
$$

$$
f = g_{j-1} + \cdots + g_1 + g_0 + f_0
$$

This illustrates that a function in the space V_j, which has a high resolution, can be successively decomposed into coarser and coarser correction components in the spaces W_{j-1} to W_0, with a remainder in the space V_0. We remark that this decomposition of a function from V_j to $V_{j-1} \oplus W_{j-1}$ will be very fast, the complexity of the operation is proportional to the number n of basis functions in V_j as the operator is a convolution between the sequence of coefficients for the basis functions in V_j and a filter whose length depends on the particular choice of wavelet basis.

That this is fast is due to the compactness of the support of the scaling function and the wavelet, for since $\phi \in V_0$, $V_0 \subset V_1$ and $\{\phi(x-k)|\forall k \in \mathbb{Z}\}$ is a Riesz basis of V_0, there exist sequences (h_k) and (g_k) such that

$$
\begin{aligned}
\phi(x) &= 2\sum_k h_k \phi(2x-k), \\
\psi(x) &= 2\sum_k g_k \phi(2x-k),
\end{aligned}
$$

and when the supports of ϕ and ψ are compact, only a finite number of the coefficients h_k and g_k are non-zero. (These are the so-called *dilation equations*.)

This is an important feature because the decomposition/reconstruction sequences will have to be applied for decomposition of the functions K, H and H_D in (12) and (13), in the steps of the iterative solution of the resultant linear system (discussed in Section 4) and possibly in the final reconstruction of the solution.

The multiresolution analysis provides us with a convenient space and a corresponding basis,

$$L^2 = \lim_{j\to\infty} V_j = \bigoplus_{j=-\infty}^{\infty} W_j = \text{span}\,\{\psi_k^j\}_{k,j=-\infty}^{\infty},$$

which we truncate to get our approximation space V_J,

$$V_J = \bigoplus_{j=-\infty}^{J-1} W_j = \bigoplus_{j=0}^{J-1} W_j \oplus V_0 = \text{span}\,\{\phi_k^0, \psi_k^0, \psi_k^1, \ldots, \psi_k^{J-1}\}_{k=-\infty}^{\infty}.$$

For problems naturally defined on an interval, we modify the construction to give the proper approximation space, see Mørken and Nygaard [6], Cohen *et al.* [11].

Appendix B. Approximation in wavelet spaces

In order to solve the integral equations (12) and (13), we have to find the coefficients $c_{H,k}^J$ and $c_{J,k,l}$ defined in (34) and (35). Alternatively, as discussed in Section 5, we may want to compute the coefficients $\boldsymbol{d}_H^j$, $\boldsymbol{c}_H^0$ in (24) and $c_{0,k,l}$, $d_{j,k,l}^h$, $d_{j,k,l}^v$ and $d_{j,k,l}^d$ in (30)–(33) for $j > 0$ more directly. Computation of the coefficients $\boldsymbol{d}_H^j$, $d_{j,k,l}^h$, $d_{j,k,l}^v$ and $d_{j,k,l}^d$ can be done by computing the involved c-coefficients on the next finer level $j+1$, and then perform the fast decomposition once. Computing coefficients $c_{j,k,l}$ in the two-dimensional case is done by a generalisation of the procedure for computing coefficients $c_{j,k}$ in the one-dimensional case. Assume that we have a biorthogonal multiresolution analysis, and a function $f \in V_j$. (For the case of an orthogonal multiresolution analysis, the multiresolution analysis is its own dual.) Taking the inner product $\langle f, g\rangle \equiv \int_0^1 f(t)g(t)\,\mathrm{d}t$ of $f = \sum c_l^j \phi_l^j \in V$ and a basis function $\tilde{\phi}_k^j$ of the dual space $\tilde{V}_j$, we get

$$\langle f, \tilde{\phi}_k^j\rangle = \langle \sum_l c_l^j \phi_l^j, \tilde{\phi}_k^j\rangle = \sum_l c_l^j \langle \phi_l^j, \tilde{\phi}_k^j\rangle = c_k^j. \tag{B1}$$

To find an approximation $\hat{f}$ of $f \in V_j$, we have to compute approximations $\hat{c}_k^j$ to the coefficients

$$c_k^j = \langle f, \tilde{\phi}_k^j\rangle = \int f(x)\tilde{\phi}_k^j(x)\,\mathrm{d}x = 2^{j/2}\int f(x)\tilde{\phi}(2^j x - k)\,\mathrm{d}x \tag{B2}$$

$$= 2^{-j/2}\int f(2^{-j}(x+k))\tilde{\phi}(x)\,\mathrm{d}x \tag{B3}$$

By using a quadrature rule for the numerical integration, we find an approximation

$$c_k^j \approx \hat{c}_k^j = 2^{-j/2}\sum_{i=1}^{n} w_i f(2^{-j}(x_i + k)). \tag{B4}$$

There are various options for how to choose the weights w_i and nodes x_i of the quadrature rule. Assuming f is smooth enough, one might try to find a Guass quadrature making the integral exact for polynomials up to a certain degree. One problem with this is that the function $\tilde{\phi}$ not necessarily satisfy the criteria for the existence of such a quadrature for a given order. Another drawback is that a new set of n evaluations of f has to be performed for each coefficient $\hat{c}_k^j$. We have used a number of n uniformly spaced nodes with spacing such that some of the evaluations for the computation of $\hat{c}_k^j$ can be reused in the computation for $\hat{c}_{k+\Delta k}^j$. For $x_i = x_0 + i$, we see that

$$2^{-j}\,(x_i + (k+1)) = 2^{-j}\,(x_{i+1} + k) \tag{B5}$$

so that in this case only one new evaluation for each new $\hat{c}_k^j$ is necessary. For f smooth, we see that

$$c_k^j - \hat{c}_k^j = 2^{-j/2}\left(2^{-j(n+1)}\int \frac{f^{(n+1)}(2^{-j}(x+k))}{(n+1)!}\tilde{\phi}(x)\,\mathrm{d}x + \cdots\right)$$

making the relative error of this quadrature

$$\frac{|c_k^j - \hat{c}_k^j|}{|c_k^j|} = \mathcal{O}(h^{n+1}), \tag{B6}$$

where $h = 2^{-j}$.

7.1. Numerical integration of non-smooth functions

Assume given a function $f \in L^2(\mathcal{R})$, where

$$f = \sum_k c_k^j \phi_k^j + \sum_{k,j'=j,j+1,\ldots} d_k^{j'}\psi_k^{j'} = \sum_k (\hat{c}_k^j + \varepsilon_k^j)\phi_k^j + \sum_{k,j'=j,j+1,\ldots} d_k^{j'}\psi_k^{j'}$$

is a wavelet decomposition of the function. What we seek are the coefficients c_k^j. We have seen that we may compute $\hat{c}_k^j$ by means of a quadrature with n uniform nodes, and if we use these as approximations to c_k^j, we make an error ε_k^j, which is of the order $\mathcal{O}(h^{n+1})$, assuming that f is sufficiently smooth. ($f \in C^n$) Here, $h = 2^{-j}$. If we now decompose f with $V_{j+\Delta j}$ as the coarsest space, we get

$$f = \sum_k c_k^{j+\Delta j}\phi_k^{j+\Delta j} + \sum_{k,j'\geq j+\Delta j} d_k^{j'}\psi_k^{j'} = \sum_k (\tilde{c}_k^{j+\Delta j} + \varepsilon_k^{j+\Delta j})\phi_k^{j+\Delta j} + \sum_{k,j'\geq j+\Delta j} d_k^{j'}\psi_k^{j'}.$$

The setting is just as above, with the difference that the level is now $j + \Delta j$ instead of j, so $\varepsilon_k^{j+\Delta j}$ is of order

$$\mathcal{O}((h/2^{\Delta j})^{n+1}) = \mathcal{O}((2^{-j-\Delta j})^{n+1}) = \mathcal{O}((2^{-j(1+\Delta j/j)})^{n+1}) = \mathcal{O}(h^{(1+\Delta j/j)(n+1)}).$$

By decomposing the error $\sum_k \varepsilon_k^{j+\Delta j}\phi_k^{j+\Delta j}(x)$ Δj times, we get the components (of the error) in the spaces W_j to $W_{j+\Delta j-1}$, spanned by all $\{\psi_k^j(x)\}_k, \ldots, \{\psi_k^{j+\Delta j-1}(x)\}_k$, and in addition, a remainder in V_j, which is spanned by $\{\phi_k^j(x)\}_k$. This remainder is of the same order as $\sum_k \varepsilon_k^{j+\Delta j}\phi_k^{j+t}(x)$ because no further error (apart from roundoff errors etc.) is introduced by the decomposition. Let this remainder be called $\sum_k \varepsilon_k^j \phi_k^j(x)$. Thus, we may write

$$\sum_k \varepsilon_k^{j+\Delta j}\phi_k^{j+\Delta j} = \sum_k \varepsilon_k^j \phi_k^j + \sum_{k,j'=j,\ldots,j+\Delta j-1} \gamma_k^{j'}\psi_k^{j'},$$

where $\gamma_k^{\cdot}$ is used to denote the parts of the error in the W-spaces. Let us likewise decompose the actually computed approximations, getting

$$\sum_k \tilde{c}_k^{j+\Delta j}\phi_k^{j+\Delta j} = \sum_k \tilde{c}_k^j \phi_k^j + \sum_{k,j'=j,\ldots,j+\Delta j-1} \tilde{d}_k^{j'}\psi_k^{j'}.$$

We can now write

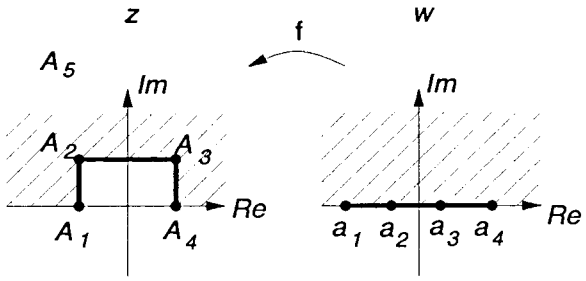

Figure 14. The conformal mapping f from the w-plane to the z-plane.

$$f = \sum_k c_k^j \phi_k^j + \sum_{k,j' \geq j} d_k^{j'} \psi_k^{j'} = \sum_k (\tilde{c}_k^j + \varepsilon_k^j)\phi_k^j + \sum_{k,j' \geq j} \ldots \psi_k^{j'},$$

where the last term indicates something in the W-spaces that we are not really interested in. The error we make by using $\tilde{c}_k^j$ as an approximation to c_k^j is therefore of order

$$\mathcal{O}(h^{(1+t/j)(r+1)}).$$

The price we have to pay is that we need $2^{\Delta j}$ times as many evaluations of f as a quadrature with r nodes would require.

Appendix C. Schwarz-Christoffel solution for flow around a square cylinder

For the square cylinder (geometry A) in an unbounded fluid, corresponding to letting $\nu = 0$ in (14), we have compared the results of the higher order methods to the solution obtained by a Schwarz-Christoffel transformation, see e.g. Kober [16], part IV. The half-plane $\mathrm{Im}(w) \geq 0$ is transformed by the conformal Schwarz–Christoffel mapping f onto the area above the piecewise straight line from $\mathfrak{Re}(z) = -\infty$ through the vertices $\{A_1 = -1, A_2 = -1+i, A_3 = 1+i, A_4 = 1\}$ and to $\mathfrak{Re}(z) = \infty$, see Figure 14. The mapping f is then given by

$$\frac{\mathrm{d}f}{\mathrm{d}w} = \prod_{j=1}^{4} (w - a_j)^{-\alpha_j/\pi},$$

where the parameters $\{a_1, a_2, a_3, a_4\}$ satisfy the conditions

$$-\infty < a_1 < a_2 < a_3 < a_4 < \infty$$

$$A_j = f(a_j),\ j = 1, \ldots, 4$$

$$\infty = f(\infty)$$

and α_j is the change of direction (in radians, counter-clockwise) in A_j when traversing the piecewise straight line from left to right. Then $\alpha_1 = \alpha_4 = \pi/2$ and $\alpha_2 = \alpha_3 = -\pi/2$. For the solution of the 'parameter problem', *i.e.*, computing the unknowns a_j, $j = 1, \ldots, 4$, we note that one of the parameters may be chosen arbitrarily, and that $|a_4 - a_3| = |a_2 - a_1|$. One numerical solution is

$$\begin{aligned} a_1 &= -0{\cdot}69142660835567 \\ a_2 &= 0 \\ a_3 &= 3{\cdot}33850670375772 \\ a_4 &= 4{\cdot}02993331211339. \end{aligned}$$

Now, if the potential for the flow in the w-plane is $\hat{\phi}(w)$, then the corresponding potential for the flow with the same boundary conditions in the z-plane will be $\phi(z) = \hat{\phi}(f^{-1}(z))$, or $\phi(f(w)) = \hat{\phi}(w)$.

References

1. B. Büchmann, J. Skourup, and H. F. Cheung, Run-up on a structure due to second-order waves and a current in a numerical wave tank. *Appl. Ocean Res.* 20 (1998) 297–308.
2. S. Finne and J. Grue, On the complete radiation-diffraction problem and wave-drift damping of marine bodies in the yaw mode of motion. *J. Fluid Mech.* 357 (1998) 289–320.
3. J. N. Newman and C. H. Lee, Sensitivity of wave loads to the discretization of bodies. In: M. H. Patel and R. Gibbins (Eds), *Proc. 6th Int. Conf. Behaviour of Offshore Structures (BOSS '92)*. London: BPP Technical Services Ltd. (1992) 50–64.
4. C. H. Lee, H. D. Maniar, J. N. Newman, and X. Zhu, Computations of wave loads using a b-spline panel method. *Twenty-first Symp. Naval Hydrodyn.* (1996) 75–92.
5. H. D. Maniar and J. N. Newman, Wave diffraction by a long array of cylinders. *J. Fluid Mech.* 339 (1997) 309–330.
6. K. Mørken and J. O. Nygaard, Biorthogonal spline wavelets on an interval. *Preprint. Dept. of Informatics, Univ. of Oslo.* (2000) 35 pp.
7. G. Beylkin, R. Coifman, and V. Rokhlin, Fast wavelet transforms and numerical algorithms i. *Communications on Pure and Applied Mathematics* XLIV (1991) 141–183.
8. J. W. Wehausen and E. V. Laitone, Surface waves. In: S. Flugge, editor, *Fluid Dynamics III, Encyclopedia of Physics*. Berlin, Göttingen, Heidelberg: Springer-Verlag (1960) 446–778.
9. I. Daubechies, *Ten Lectures on Wavelets*. CBMS-NFS Regional conference series in applied mathematics. Philadelphia, Pennsylvania: SIAM (1992) 352 pp.
10. B. Jawerth and W. Sweldens, An overview of wavelet based multiresolution analyses. *SIAM Rev.* 36 (1994) 377–412.
11. A. Cohen, I. Daubechies, and P. Vial, Wavelets on the interval and fast wavelet transforms. *Appl. Comp. Harmonic Anal.* 1 (1993) 54–81.
12. W. Sweldens, The lifting scheme: A construction of second generation wavelets. Preprint, retrieved by ftp (`http://cm.bell-labs.com/who/wim/papers/`) (1995).
13. W. Sweldens and P. Schröder, Building your own wavelets at home. Retrieved by ftp (`http://cm.bell-labs.com/who/wim/papers/`) (1995).
14. A. M. Bruaset, *A survey of preconditioned iterative methods*. Pitman Research Notes in Mathematics. Essex, UK: Longman Scientific & Technical (1995) 159 pp.
15. J. N. Newman and P. D. Sclavounos, Large-scale computation of wave loads on offshore structures. In: Faltinsen *et al.* (Ed.), *Proc. 5th Int. Conf. Behaviour of Offshore Structures (BOSS '88)*. Trondheim, Norway: Tapir (1988) 1–15.
16. H. Kober, *Dictionary of Conformal Representations*. USA: Dover (1952) 208 pp.